**NASA TECHNICAL MEMORANDUM**

NASA TM X-71852

NASA TM X-71852

(NASA-TM-X-71852) HOT ION PLASMA PRODUCTION IN HIP-1 USING WATER-COOLED HOLLOW CATHODES (NASA) 57 p HC $4.50 CSCL 20I
N76-16931
Unclas
G3/75 13675

# HOT ION PLASMA PRODUCTION IN HIP-1 USING WATER-COOLED HOLLOW CATHODES

by J. J. Reinmann, M. R. Lauver, R. W. Patch,
R. W. Layman, and A. Snyder
Lewis Research Center
Cleveland, Ohio 44135

TECHNICAL PAPER presented at
Seventeenth Annual Meeting of the Division of Plasma
Physics of the American Physical Society
St. Petersburg, Florida, November 10-14, 1975

# ABSTRACT

Further hot-ion plasma experiments were conducted in the NASA Lewis HIP-1 magnetic mirror facility. A steady-state $\underline{E} \times \underline{B}$ plasma was formed by applying a strong radially inward dc electric field near the mirror throats. Most of the results were for hydrogen, but deuterium and helium plasmas were also studied. Three water-cooled hollow cathodes were operated in the hot-ion plasma mode with the following results: (1) thermally emitting cathodes were not required to achieve the hot-ion mode; (2) steady-state operation (several minutes) was attained; (3) input powers greater than 40 kW were achieved; (4) cathode outside diameters were increased from 1.2 cm (uncooled) to 4.4 cm (water-cooled); (5) steady-state hydrogen plasmas with ion temperatures from 185 to 770 eV and electron temperatures from 5 to 21 eV were produced. Plasma discharge I-V characteristics were determined. Scaling relations were empirically obtained for discharge current, ion temperature, electron temperature, and relative ion density as a function of hydrogen gas feed rate, magnetic field, and cathode voltage. Neutrons were produced from deuterium plasmas, but it was not established whether they came from the plasma volume or from the electrode surfaces.

E-8588

# HOT ION PLASMA PRODUCTION IN HIP-1 USING WATER-COOLED HOLLOW CATHODES

by J. J. Reinmann, M. R. Lauver, R. W. Patch,
R. W. Layman, and A. Snyder

Lewis Research Center

## SUMMARY

Further hot-ion plasma experiments were conducted in the NASA Lewis HIP-1 magnetic mirror facility. A steady-state $\underline{E} \times \underline{B}$ plasma was formed by applying a strong radially inward dc electric field near the mirror throats. Most of the results were for hydrogen, but deuterium and helium plasmas were also studied. Three water-cooled hollow cathodes were operated in the hot-ion plasma mode with the following results: (1) thermally emitting cathodes were not required to achieve the hot-ion mode; (2) steady-state operation (several minutes) was attained; (3) input powers greater than 40 kW were achieved; (4) cathode outside diameters were increased from 1.2 cm (uncooled) to 4.4 cm (water-cooled); (5) steady-state hydrogen plasmas with ion temperatures from 185 to 770 eV and electron temperatures from 5 to 21 eV were produced. Plasma discharge I-V characteristics were determined. Scaling relations were empirically obtained for discharge current, ion temperature, electron temperature, and relative ion density as a function of hydrogen gas feed rate, magnetic field, and cathode voltage. Neutrons were produced from deuterium plasmas, but it was not established whether they came from the plasma volume or from the electrode surfaces.

# INTRODUCTION

This report presents further results of the hot-ion plasma experiments conducted in the HIP-1 facility at the NASA Lewis Research Center (LeRC) (refs. 1 and 2). HIP-1 is a water-cooled magnetic mirror facility with a mirror ratio of 1.82 and maximum magnetic flux density of 2.15 tesla at the mirrors. A steady-state plasma is formed by applying a radially inward dc electric field (several kV/cm) near the throats of the mirrors. The mutually perpendicular electric and magnetic fields cause the plasma to rotate (drift) in the azimuthal direction. This azimuthal motion provides a kinetic energy input, predominantly to the ions. Randomization of this energy and enhancement of ion heating may be due primarily to oscillations (refs. 3 and 4). In previous experiments conducted in SUMMA (Superconducting Magnetic Mirror Apparatus) at LeRC (refs. 5 and 6), this plasma heating process produced ion temperatures in the kilovolt range for hydrogen and helium plasmas.

The purpose of this report is to document the results of the first application of water-cooled hollow cathodes to this heating process. Water-cooled anodes and floating shields were first developed in SUMMA to prevent the electrodes from melting at high power inputs (refs. 5 and 7). The cathodes in SUMMA were not water-cooled, but they could absorb the high power input without melting because they were made of tungsten. However, long-term steady-state operation required a heat removal process that was more effective than the simple conduction and radiation processes employed in the uncooled tungsten cathodes.

The principal diagnostic tool used in this investigation was an optical monochromator to estimate ion temperatures and relative ion density via Doppler line broadening, and electron temperatures via line-intensity-ratio techniques. Neutron production in deuterium plasmas was also monitored.

The reproducible, steady-state performance of the completely water-cooled electrode system in HIP-1 has permitted a careful documentation of the plasma discharge. Current versus voltage characteristics, and preliminary scaling relations for the dependent variables as a function of the independent variables are reported for the first time. Simple power law relations were assumed for the scaling relations. The scaling relations were obtained only for hydrogen plasmas, but deuterium and helium plasmas were also produced with the water-cooled cathodes.

Three water-cooled cathode geometries, ranging in outside diameter from 2.9 to 4.4 cm, were tested. The previously used uncooled tungsten cathodes were 1.27 cm in outside diameter (ref. 2).

## APPARATUS

The HIP-1 facility was constructed at NASA Lewis Research Center to develop a hot-ion plasma source for use in thermonuclear research. It is operated from a control room adjacent to the test cell. The magnets and test section have been described briefly in reference 2.

### Magnet

Two water-cooled copper solenoids serve as mirror magnets. They produce a maximum steady field of 1.18 T at the midplane of the test section and 2.15 T at the mirrors (mirror ratio of 1.82).

### Plasma Test Section

A schematic view of the plasma test section and magnet configuration is shown in figure 1. The test section is a water-cooled cylinder made of type 304 stainless steel. Its inner diameter is 25 cm and its length is 1.63 m. Diffusion pumps at each end of the test section evacuate it to a base pressure of about $5\times10^{-7}$ torr.

A quartz window at each end port of the test section provides a good view, via a mirror, of the plasma and electrodes. Quartz or borosilicate glass windows on the midplane ports provide access for the monochromator diagnostics and for direct visual observation of the plasma.

## Facility Instrumentation

A schematic of the gas fuel system is presented in figure 2. The flow meters and a magnetically shielded ion gauge on the test section have remote readouts in the control room. Variable leak valves are used in conjunction with two pressure regulators to set the mass flow rates at the east and west hollow-cathodes and at the test-section midplane.

A schematic of the electrode high-voltage circuit is given in figure 3. The primary power supplies (rated at 10 kV, 10 A each) were connected in series. They were operated successfully up to 23 kV. An on-off high-voltage vacuum switch, mounted in one of the power supply cabinets, is operated remotely from the control room. The cathode currents were measured with floated ammeters. Cathode currents were also measured remotely from the control room with high-voltage-isolated dc current sensors. At higher currents and voltages, the dc current sensors gave grossly inaccurate readings due to r.f.i. plasma noise. The anode currents were also measured remotely from the control room with one ohm current shunts.

## Electrode Assembly

The location of the anodes, cathodes, and electrically floating shields are shown in figure 1. A photograph of an electrode assembly is shown in figure 4. A magnetic field-line plot is superimposed on the outlines of the electrodes and test section in figure 5. The anodes were located 2.8 cm outside the mirrors. The cathode tips were located about 7.7 cm from the anode midplane. (We have not established an optimum location for the anodes and cathodes within the mirror throats.) A photograph of the uncooled tungsten cathode and three water-cooled cathodes are shown in figure 6 and cut-away views of the cathodes are shown in figure 7. The three water-cooled cathodes are referred to as no. 1, no. 2, and no. 3 in the order of increasing inner diameter. These cathodes were fabricated (ref. 8) from standard copper tubing and tube fittings and from simply machined parts for the water distributors near the tips.

In each water-cooled cathode, a tube fed cooling water into a small chamber between the distributor plate and the tip face of the cathode. Multiple small holes in the distributor plate allowed the water to circulate back to an exhaust tube, cooling the walls. With this construction the coldest water always circulated across the face of the cathode. The 13 mm stem piece was fabricated from stainless steel. The pieces were silver soldered or brazed together.

The water-cooled anodes were helixes wound with two loops of copper tubing. Table I lists the pertinent dimensions for the corresponding cathode-anode pairs. The dimensions of the annular gap between the cathode and anode were based on past experience, but they were not necessarily optimum.

The electrically floating shields, which were also water-cooled, protect the cathode support insulators from charge-exchange and ion bombardment, and prevent arcing along magnetic field lines from cathode to ground.

Most water-cooled electrode components were fabricated from copper. To minimize sputtering, the copper surfaces exposed to energetic plasma were coated with tungsten via a commercial plasma flame-spraying process.

Whenever a major change was made in the electrodes or in the test-section interior, a break-in or conditioning period of hours to days of operation was required to obtain high-voltage high-current operation without excessive arcing. Conditioning periods were longest for those parts that had a large surface area with tiny, sharp-pointed surface irregularities such as the tungsten flame-sprayed electrodes.

# PLASMA DIAGNOSTICS

## Optical Spectroscopic Diagnostics

Apparatus. - The emission spectroscopy apparatus for determining ion and electron temperatures is shown in figure 8. It was located at the test-section midplane and viewed the plasma perpendicular to the magnet axis. The vertical centerplane (defined as a vertical plane containing the magnet axis) was focused on the entrance slit of the monochromator with a lens. Between the lens and the entrance slit the beam was rotated 90° with a beam rotator. A stop was provided to reduce the vertical height of the beam. The beam cross-section at the vertical centerplane was determined by the size and shape of the entrance slit. The beam cross-section was approximately 2 mm in the vertical direction and 26 mm parallel to the magnet axis. An adjustable screw at the base of the monochromator stand was used to make vertical scans (fig. 8). For the work reported here the monochromator was focused across the centerline of the plasma so the quantity $y$ in figure 8 was zero. The grating monochromator employed an f/8.6 1/2 m Ebert mounting with curved slits. The reciprocal linear dispersion was 1.6 nm/mm in first order. A photomultiplier with extended S-20 photocathode was used for detection. It was magnetically shielded and cooled with air that came from a vortex tube refrigerator.

Ion temperature, relative ion density, and charge-exchange loss determination. - Observations of the Doppler-broadened Balmer $H_\alpha$ line emission were used to obtain a chordal average of the ion temperature and the relative ion density at the midplane. Figure 9 shows a typical $H_\alpha$ line profile taken in HIP-1. There is an intense narrow component due to electronic excitation of cold and Franck-Condon neutrals. The wide component was assumed to be due primarily to simultaneous electronic excitation and charge exchange by the reaction

$$H_f^+ + H_2 \rightarrow H_f(n = 3) + H_2^+ \qquad \text{(I)}$$

where the subscript f stands for "fast" and n is the principal quantum number. The emission spectra from $H_f(n = 3)$ is Doppler broadened because the $H_f$ has essentially the same velocity as $H_f^+$. Hence the width (or second moment) of the wide component of the $H_\alpha$ line was used to obtain the $H_f^+$ ion temperature averaged across the midplane diameter. The ion temperatures were obtained by the methods described in reference 9 where it was assumed that reaction (I) predominates. Reaction (I) will predominate if the plasma is small in size and has a low enough electron density (roughly $10^{12}$ cm$^{-3}$ for a 5 cm diameter plasma), and the following reactions can be neglected.

$$H_f^+ + H \rightarrow H_f(n = 3) + H^+ \qquad \text{(II)}$$

$$H_{2f}^+ + H_2 \rightarrow H_f(n = 3) + H(n = 1) + H_2^+ \qquad \text{(III)}$$

$$H_{2f}^+ + H \rightarrow H_f(n = 3) + H_2^+ \qquad \text{(IV)}$$

Reactions (II) and (IV) can be neglected if the degree of dissociation of $H_2$ to H is small. In the present experiment $H_2$ is fed in at the cathodes and is also created by recombination on the metal walls. Approximate calculations showed that the mean free path for the disappearance of $H_2$ was the same order of magnitude as the plasma radius. Since $H_2$ originates both at the cathodes and at the walls it was assumed that the degree of dissociation to H was small. Reaction (III) can be neglected if the number density of $H_2^+$ is much less than the number density of $H^+$ (reaction (III) has a larger cross-section than reaction (I) (ref. 10)). Both the neutral particle spectrometer results (refs. 2 and 5) and an approximate composition calculation indicate that $H_2^+$ is present in the HIP-1 plasma. The $H_2^+$ density was estimated to be less than 15 percent of the $H_1^+$ density. Thus, the neglect of reaction (III) needs further study.

The wide components of the $H_\alpha$ line are also useful for estimating a relative value of the product of ion density and neutral density averaged across a chord. The rate of production of $H_\alpha$ wide-component photons is assumed proportional to $\bar{n}_o \bar{n}_i \langle \overline{\sigma_\alpha v_i} \rangle$, where the symbols are defined in the APPENDIX. Hence the area A of the wide component curve of figure 9 is given by the proportionality

$$A \propto \bar{n}_o \bar{n}_i \langle \overline{\sigma_\alpha v_i} \rangle \tag{1}$$

or

$$\bar{n}_o \bar{n}_i \propto \frac{A}{\langle \overline{\sigma_\alpha v_i} \rangle} \tag{2}$$

In the absence of a plasma the test-section pressure was proportional to the gas feed rate G. If it is further assumed that $\bar{n}_o$ is proportional to G when plasma is present in the test section, the relative ion density $\bar{n}_i$ is obtained from equation (2) as

$$\bar{n}_i \propto \frac{A}{G \langle \overline{\sigma_\alpha v_i} \rangle} \tag{3}$$

The quantity $\langle \overline{\sigma_\alpha v_i} \rangle$ depends only on the $H^+$ ion temperature; it was calculated using the optical cross sections for reaction (I) and is shown in figure 10 as a function of ion temperature.

The power q lost from the plasma by charge exchange via reaction (I) is proportional to the quantity

$$q \propto \bar{n}_o \bar{n}_i \left\langle \overline{\sigma_{gc} v_i^3} \right\rangle \tag{4}$$

where $\sigma_{gc}$ is the charge-exchange cross section for the reaction

$$H_f^+ + H_2 \rightarrow H_f(n = 1) + H_2^+ \qquad \text{(V)}$$

It is assumed that the sum of the charge-exchange cross sections for producing electronically excited states can be neglected compared to $\sigma_{gc}$. Equation (4) also neglects charge-exchange loss by reaction (III). The cross section $\sigma_{gc}$ was obtained from references 11 and 12. Values of $\left\langle \overline{\sigma_{gc} v_i^3} \right\rangle$ are plotted as a function of $T_i$ in figure 10. Combining equations (2) and (5) gives the proportionality used for $q$

$$q \propto \frac{A \left\langle \overline{\sigma_{gc} v_i^3} \right\rangle}{\left\langle \overline{\sigma_\alpha v_i} \right\rangle} \qquad (5)$$

Electron temperature determination. - A radial average of the electron temperature was obtained by observing the emission intensities of the optically thin He 706.5 and 728.1 nanometer lines (fig. 11) and taking the ratios of the intensities (or areas) as described in reference 9. To make this measurement in hydrogen plasmas it was necessary to add 10 percent helium by volume to the hydrogen.

## Neutron Monitoring System

Because a fast neutron is non-ionizing particle, to detect the 2.45 MeV neutrons from the $D(d,n)^3He$ reaction it is necessary to utilize an intermediate reaction. Boron 10 has a high capture cross section for slow (thermal) neutrons, therefore, a Geiger tube filled with enriched (98 percent $^{10}B$) $BF_3$ was used to detect slow neutrons by the following reaction,

$$^{10}B + n \rightarrow {}^4He + {}^7L_i + Q \qquad \text{(VI)}$$

Since the alpha particle ($^4He$) is produced in the Geiger tube, it is counted indicating that a neutron has been captured.

The HIP-1 neutron monitoring system consists of 5 commercially available Geiger tubes wired in parallel (fig. 12). The tubes are embedded in a block of paraffin 20 cm × 20 cm × 30 cm; the purpose of the paraffin is to thermalize the neutrons so they will be captured by the $^{10}B$ in the Geiger tubes. A several MeV neutron is slowed to thermal velocities (0.025 eV) in about 50 successive collisions with protons.

The output of the Geiger tubes goes to a preamplifier and then to a scaler. The high voltage power supply is incorporated in the scaler chassis. A timer gates the scaler on for a preselected counting time.

To calibrate the system, a Californium 252 neutron source of known activity was used. The source was placed inside the test section at the midplane. The detector assembly was placed under the HIP-1 facility at the midplane. With the axes of the Geiger tubes oriented perpendicular to the magnetic field lines, the counting rate did not change when the midplane magnetic field was varied from zero to 1.1 T. This calibration provided an approximate attenuation factor from source to counter so that the actual neutron production rate in HIP-1 could be estimated.

## DISCUSSION OF RESULTS

### Current Versus Voltage Characteristics of the Plasma Discharge

Figure 13 shows two hydrogen discharge I-V curves for the HIP-1 hot ion plasma process. The lower curve is typical of operation at either low magnetic fields or low gas feed rates. The upper curve is for operation at either high magnetic fields or high gas feed rates. Gas was fed through the hollow cathodes. The voltage applied to the cathodes was the independent variable and the current was the dependent variable. The current refers to the power supply current, which was equal to the sum of the cathode currents. For the data reported here the sum of the anode currents was also equal to the power supply currents.

There are two fairly distinct plasma modes revealed in the upper curve of figure 13. At low voltages the I-V curve was fairly steep: this is referred to as the low-resistance mode. At higher voltages the I-V curve was almost flat: this is referred to as the high-resistance ion-heating mode. In the region near and just to the right of the peak of the curve, the plasma developed a low frequency (60 to 100 Hz) unstable operating mode. At higher values of current (associated with higher gas flow rate and/or magnetic field) the cathode voltage oscillation became a significant fraction of the dc voltage level. The oscillation was probably reinforced by the operating point moving back and forth across the sharp current peak. Since the power supplies were filtered for 360 Hz (with a normal 360 Hz ripple of 1.5 percent), the 60 to 100 Hz oscillation was almost uncontrollable. Therefore, operation near the peak was avoided. This may be a feedback interaction between the power supply and the plasma. Therefore the shape of the I-V curve near the peak might be altered if lower frequencies were properly filtered in the power supply. These low frequency oscillations have also been observed when there was inadequate pumping speed. The plasma exhibited visible low frequency flickering when the number of vacuum pumps was reduced. As the number of vacuum pumps was increased, the gas flow rate had to be increased to maintain the same current, but the plasma ran steadier.

At lower gas flow rates and/or magnetic fields, there was a smooth transition (low frequency oscillations were absent) from the low-resistance to the high-resistance mode as the applied voltage was increased (see lower curve of fig. 13).

Most of the results reported herein were taken in the high-resistance ion-heating mode. In this mode the hydrogen plasma was characterized by an annular halo at the midplane of the magnetic mirror (fig. 14); inside the halo was a cylindrical column of plasma that conformed to the magnetic field lines that are tangent to the internal diameter of the anode rings. The narrow halo glow at the midplane is probably due to ions trapped with almost pure transverse velocities at the minimum-B part of the magnetic mirror (ref. 13). After a few hours of operation, the midplane viewing-port windows become coated with a layer of metal sputtered from the test section walls. But there was always a vertical stripe (about 3 cm wide) at the midplane without any metal coating. It is believed that the metal was sputtered off this stripe by the fast charge-exchange neutrals emerging from the plasma. These charge-exchange neutrals must have almost pure transverse velocity if they strike near the midplane of the viewing port which is about 36 cm from the magnetic axis. After several minutes of high power operation, the viewing port windows and their flanges become hot to the touch.

At high currents, the low-resistance mode is characterized by a bright, noisy (r.f.i.), low ion-temperature plasma in which the halo was not visible.

The general shape and characteristics of the I-V curves are about the same for either one or two anodes although detailed plasma properties may be sensitive to the number of anode rings. A comparison of ion temperatures for one-anode and two-anode operation is presented in a later section.

Effect of gas flow rate on the I-V characteristics. - Figure 15 shows a set of I-V curves with gas flow rate as the parameter and with magnetic field held constant. As seen from the curves, current was very sensitive to the gas flow rate. Actually, the current is probably sensitive to the neutral background pressure rather than the gas flow rate per se.

During steady-state operation, the current underwent a slow cyclic variation, typically from 0.7 to 1.0 A (with a period of a fraction of a minute to minutes). The data was usually taken at the minimum current point. The test section pressure was observed to vary in phase with the current. The cause of the pressure variations have not yet been explored.

Effect of magnetic field on the I-V characteristics. - Figure 16 shows a set of I-V curves with midplane magnetic field as the parameter and with gas flow rate held constant. Comparing figures 15 and 16 it is observed that both magnetic field and gas flow rate have the same qualitative effect on the I-V characteristics. As with gas flow rate, the current increased with increasing magnetic field over most of the voltage range. Actually at low voltages the current decreased with increasing magnetic field although it is somewhat difficult to see on figure 16.

Effect of gas feed location on the I-V characteristics. - The effect of gas feed location on the I-V characteristics at constant gas flow rate and magnetic field is illustrated in figure 17. The gas feed arrangements were: (1) east cathode gas feed only; (2) west cathode gas feed only; and (3) gas flow equally divided between the east and west cathodes. In each case the gas flow was adjusted to give an anode current of approximately one-half ampere at twenty kilovolts. Because of the extreme sensitivity of current to gas flow rate, conditions were never matched perfectly. As seen from figure 17, the gas feed location did not significantly affect the I-V characteristics as long as the gas was introduced through the hollow cathodes.

With hollow cathode feed, the discharge could be operated at any midplane magnetic field up to the limits of the magnet facility, 1.1 T. However, when the gas was introduced at the midplane of the test section wall, rather than through the cathodes, the discharge would operate at midplane magnetic fields up to about 0.9 T. At higher magnetic fields, low frequency oscillations developed ($\lesssim 60$ Hz) and the plasma ran so unsteadily that the power supply current-limit switches would trip.

## Functional Dependence Among Plasma Variables

In this experiment, the independent variables are gas feed rate, gas feed location, magnetic field, cathode voltage, vacuum pumping speed, electrode geometry, electrode cooling, and gas used to form the plasma. The dependent variables are ion temperature, ion density, neutral density, electron temperature, electric field, plasma azimuthal drift velocity, cathode currents, anode currents, other stray currents, percent dissociation, etc. Most of the dependent variables also depend on the spatial coordinates. This section shows how ion temperature, relative ion density, electron temperature, and the ratio $q/P$ scaled with mass flow, magnetic field, and cathode voltage. The electrode geometry consisted of cathodes no. 3 at both the east and west ends, and an anode ring at the west end only. Gas was fed only into the east cathode. All four vacuum pumps were used for these studies. The range covered by the independent variables was: hydrogen flow rate, 0 to 0.7 sccs; midplane magnetic field, 0.7 to 1.1 T; and cathode voltage, 13 to 22 kV. The range of data is quite limited, and therefore the interpretation and extrapolation of results must take this into account. Simple power-low relations were obtained by assuming straight-line fits to the data plotted on log-log paper.

Most of the data points that were used to obtain the functional relations were an average of at least three sets of data. Unless otherwise noted, when the plasma exhibited a slow cyclic variation in the anode current, the data were always taken at the lowest current point in the cycle.

In the following sections, functional dependences for the relative $H^+$ ion densities, $\overline{n}_i$, were determined from equation (8). To obtain equation (8), it was assumed that $n_o \propto G$. It would be more correct to present functional dependences of $\overline{n}_o\overline{n}_i$. When the functional dependencies are summarized at the end of this section, both $\overline{n}_o\overline{n}_i$ and $\overline{n}_i$ ($\overline{n}_o \propto G$) functional relations are presented.

In the following sections, the Doppler-broadened Balmer-$H_\alpha$-line-emission measurements were obtained on plasmas made with 100 percent $H_2$ gas feed; to obtain the electron temperatures it was necessary to add 10 percent helium by volume to the $H_2$ gas feed. Thus, although the results obtained from the $H_\alpha$ measurements and the results for $T_e$ are both plotted on the same figure, they came from different plasma runs.

Dependence on gas flow rate (B and V fixed). - Figure 18 is a set of log-log plots that show the dependence of $T_i$, $\overline{n}_i$, I, q/P, and $T_e$ on G with B and V held fixed. Using straight-line fits to the data of figure 18, the following functional dependences were obtained.

$$\left.\begin{array}{ll} T_i \propto G^{1.5} & \\ \bar{n}_i \propto G^{2.4} & (\bar{n}_0 \propto G) \\ I \propto G^{4.7} & \\ T_e \propto G^{-1.3} & \end{array}\right\} (B, V \text{ fixed}) \qquad \begin{array}{r} (6a) \\ (6b) \\ (6c) \\ (6d) \end{array}$$

The increasing ion temperature probably reflects the increased power input that accompanied increased gas flow rates. The decreasing electron temperature with increased gas flow rate may be because both the ion and neutral densities increased, decreasing the mean free path for electrons. Eliminating G from equations (6b) and (6c) reveals that the current increases as the square of the ion density for fixed B and V.

Dependence on midplane magnetic field (V and G fixed). - In figure 19 $T_i$, $\bar{n}_i$, I, q/P and $T_e$ are presented as a function of B with V and G held fixed. The ion temperature rises rapidly at low magnetic fields and then tends to level off. It is difficult to obtain a clear trend for $T_i$ from these results. Thus the derivation of an approximate scaling relation between $T_i$ and B will be deferred until additional results are presented for the case where voltage and current were held constant. A summary of the scaling relations from figure 19 are as follows.

$$\left.\begin{array}{ll} T_i \quad \text{not clear} & \\ \bar{n}_i \propto B^{5.6} & (\bar{n}_0 \propto G) \\ I \propto B^{4.2} & \\ T_e \propto B^{-5.9} & \end{array}\right\} (V, G \text{ fixed}) \qquad \begin{array}{r} (7a) \\ (7b) \\ (7c) \\ (7d) \end{array}$$

In figure 19 the ratio of charge-exchange power loss to input power increases fairly rapidly with increasing B. This suggests that some other loss mechanism is reduced as B increases. One obvious loss mechanism that should vary inversely with B is charged particle diffusion across magnetic field lines. Figure 32 from Appendix B shows that the mean ion residence time, $\tau_r$, increases rapidly with B.

Dependence on cathode voltage (G and B fixed). - Figures 20(a) and (b) show plots of $T_i$, $\bar{n}_i$, I, q/B and $T_e$ as a function of V with G and B held constant. Figure 20(a) is for an anode current level of about 0.5 A, and figure 20(b) is for about 1.1 A. $T_e$ was not obtained for figure 20(b). It is reassuring to note that the corresponding slopes for ion temperature at the two current levels were essentially the same; likewise for the ion density. The straight-line fits for the data of figure 20 are summarized below.

$$\left.\begin{aligned} &T_i \propto V^{1.4} && \text{(8a)}\\ &\bar{n}_i \propto V^{-3.1} \quad (\bar{n}_0 \propto G) && \text{(8b)}\\ &I \propto \text{constant} && \text{(8c)}\\ &T_e \propto V^{0.45} && \text{(8d)} \end{aligned}\right\} (G, B \text{ fixed})$$

Probably the most significant new result in this report is the negative slope (minus 3.1) for the ion density curve. (Since the cathode current does not increase strongly with cathode potential, it does not appear that the cathodes pull appreciably more ions out of the plasma as the cathode voltage is made more negative.) A drop off in ion density can be predicted from power balance considerations. For the data given in figure 20, the ratio of power lost by charge exchange to the power lost as charged-particle kinetic energy ranged from 5.7 to 9.8. This ratio is given by $\left(\frac{1}{2} m_i \left\langle \overline{\sigma_{gc} v_i^3} \right\rangle\right) \Big/ \left(\frac{3}{2} kT_i (\langle \overline{\sigma_{ie} v_e} \rangle + \langle \overline{\sigma_{ii} v_i} \rangle)\right)$ (see Appendix B for the determination of $\langle \overline{\sigma_{ie} v_e} \rangle$ and $\langle \overline{\sigma_{ii} v_i} \rangle$). If reaction (III) were also included, the above ratio would be even larger. Thus, the dominant loss mechanism seems to be volume charge exchange. The plasma energy balance therefore requires that

$$\bar{n}_o \bar{n}_i \left\langle \overline{\sigma_{gc} v_i^3} \right\rangle \propto IV = P \tag{9}$$

From figure 10 $\left\langle \overline{\sigma_{gc} v_i^3} \right\rangle$ scales as $T_i^{2.3}$ in the range of $T_i$ from 200 to 400 eV. G was constant, so $\bar{n}_o$ was assumed to be constant. Measured I was approximately constant. Using this information in equation (9) gives the following relation:

$$\bar{n}_i \propto \frac{V}{\left\langle \overline{\sigma_{gc} v_i^3} \right\rangle} \propto \frac{V}{T^{2.3}}$$

Since ion temperature scaled as $V^{1.4}$ or greater, we get

$$\bar{n}_i \propto \frac{V}{V^{3.2}} = \frac{1}{V^{2.2}} \tag{10}$$

Since $\left\langle \overline{\sigma_{gc} v_i^3} \right\rangle$ has a stronger dependence on cathode voltage (via the ion temperature) than does the input power, the steady-state ion density must decrease with increasing cathode voltage to maintain a steady-state power balance. The implications of this calculation are sufficiently important to warrant a more careful study of how power-balance requirements can affect the steady-state plasma parameters. By achieving burnout conditions, the charge-exchange loss can be reduced from a volume effect to a surface effect. By improving vacuum pumping, through the use of larger ports and possibly titanium walls, the neutral background density may be reduced which also leads to a reduction in charge-exchange cooling. We have evidence both from reference 2 and from our present studies that improved vacuum pumping does indeed improve ion temperatures, an effect that may possibly be attributed to reduced charge-exchange cooling.

In reference 3, it was suggested that ion temperature would scale as the square of the cathode voltage. This variation resulted from the simple assumptions that the ion temperature was proportional to the $\underline{E} \times \underline{B}$ drift energy of the ions, and the electric field, $\underline{E}$, was proportional to the cathode voltage. For the data shown in figure 20 the ion temperature has a slope of about 1.4. Some data taken with two anodes suggest a range of slopes from 1.4 to 2. The slope of the two-anode data increased with increasing gas flow. Further experiments are needed to clarify the effects of anode geometry and cathode voltage on ion temperature.

Two possible reasons why the electron temperature increased with cathode voltage in figure 20(a) are: (1) the electric field is stronger; and (2) the ion density decreased. Both of these effects increase the electron mean free path.

<u>Dependence on midplane magnetic field (V and I fixed).</u> - When the plasma is in operation, the only dependent variable that can be directly measured (without data reduction processes) is the anode (or cathode) current. Therefore, it was possible to experimentally determine the effect of varying B while maintaining constant I and V. This was done by readjusting G for each new B setting. Figure 21 shows how the various plasma parameters vary with B when V and I (anode current) are held constant. Using straight-line fits to the data in figure 21, we obtain the following dependences:

$$\left.\begin{aligned} & T_i \propto B^{-0.77} && && \text{(11a)} \\ & \bar{n}_i \propto B^{2.83} && (\bar{n}_0 \propto G) && \text{(11b)} \\ & G \propto B^{-0.67} && && \text{(11c)} \end{aligned}\right\} \text{(I, V fixed)}$$

Electron temperatures were not obtained for these conditions. The ion density dependence is somewhat better than the $B^2$ relation predicted by the analysis of reference 3. In reference 3, a dispersion relation predicting the onset of the lower hybrid ion heating instability was used to obtain the $B^2$ scaling law. That analysis did not consider all the possible independent variables that could affect ion density. It has also been suggested (ref. 3) that the random ion energy is proportional to the $\underline{E} \times \underline{B}$ drift energy which would make $T_i$ scale as $1/B^2$.

The ratio of charge-exchange power loss to power input increased with increasing magnetic field. This again suggests that some other power loss mechanism (such as charged particle diffusion) decreases as the magnetic field is increased.

*Summary of functional dependences and their implications.* - The *simple* and *approximate* scaling relations obtained from figures 18 through 21 are summarized below.

$$T_i \propto G^{1.5} B^{a} V^{1.4} \tag{12a}$$

$$\bar{n}_i \propto G^{2.4} B^{5.6} V^{-3.1} \qquad (n_o \propto G) \tag{12b}$$

$$\bar{n}_o \bar{n}_i \propto G^{3.4} B^{5.6} V^{-3.1} \tag{12c}$$

$$I \propto G^{4.7} B^{4.2} \tag{12d}$$

$$T_e \propto G^{-1.3} B^{-5.9} V^{0.45} \tag{12e}$$

The value of $\underline{a}$ in equation (12a) is *estimated* by comparing the relations given in equations (11) and (12). Eliminating G between equations (12a) and (12c) gives

$$T_i \propto I^{0.32} B^{a-1.34} V^{1.4} \tag{13}$$

Equating the powers of B in equations (11a) and (13) (note that I and V are fixed in equation (11a)), we obtain $a = 0.57$. Thus the approximate expression for $T_i$ is

$$T_i \propto G^{1.5}B^{0.6}V^{1.4} \tag{14}$$

Current, magnetic field, and cathode voltage are the parameters that closely relate to the experimental hardware limits. Ion temperature, electron temperature, and relative ion density can be expressed in terms of I, B, and V by using equation (12d) to eliminate G from equations (14), (12b), (12c), and (12e). These manipulations yield the following relations

$$T_i \propto I^{0.3}B^{-0.8}V^{1.4} \tag{15a}$$

$$\bar{n}_i \propto I^{0.5}B^{3.5}V^{-3.1} \tag{15b}$$

$$\bar{n}_o\bar{n}_i \propto I^{0.7}B^{2.6}V^{-3.1} \tag{15c}$$

$$T_e \propto I^{-0.3}B^{-4.7}V^{0.45} \tag{15d}$$

When equations (15) are compared with equations (11), they are not mathematically self-consistent. However, the trends expressed in both sets of equations are in agreement. These disparities are not unexpected in view of the approximate nature of these power law relations.

Depending on the applications for this plasma, various combinations of the values of $n_i$, $T_i$, and $T_e$ may be desired. Scaling relations, such as those developed here, should prove useful in achieving these requirements. These relations should also prove useful in formulating a physical model of the plasma.

Application of functional relations to HIP-1 results. - The scaling relations for $T_i$ and $T_e$, equations (15a) and (15d) respectively, were applied to all the data taken on the water-cooled cathodes no. 3 with one anode. The results for $T_e$ are plotted on figure 22 and those for $T_i$ are found on figure 23. The correlations were fairly successful in pulling the data together along straight lines that pass through the origin. The scaling relation for $T_i$ is applied to the data for other cathode-anode geometries in the next section.

For similar hot-ion plasma experiments conducted in SUMMA (ref. 5), $T_i$ was found to correlate rather loosely with the quantity VI/B. The $T_i$ results for the water-cooled cathodes reported here for HIP-1 did not correlate with VI/B. We have not yet attempted to apply equation (15a) to the SUMMA data.

The effect of cathode and anode geometry on ion temperatures. - In our tests heretofore, we used a matched pair of anodes and cathodes at each mirror throat. The need for two anodes was questioned because the electrical conductivity along magnetic field lines was believed sufficient to maintain the same plasma potential distribution and hence the same ion heating by $\underline{E} \times \underline{B}$ effects with either one or two anodes. Therefore, tests were made with water-cooled cathodes no. 3 to compare the ion temperatures produced with one and two anodes. The single anode was operated in its usual location. One-anode operation was as stable over as wide an operating range of current, voltage, and magnetic flux density as two-anode operation. Figure 23, (presented in the last section), shows the ion temperature results for one anode. Figure 24, shows the ion temperature results for two anodes. Again the data cluster along a straight line passing through the origin. However, the slope for the two anode line is about twenty percent greater than the slope for the one anode line. These results reveal that ion heating is more effective with two anodes than with one anode. This indicates that anode geometry effects should be more completely explored.

Ion temperatures obtained from the tests of water-cooled cathodes no. 1 and 2 were also plotted against the scaling parameter given by equation (15a). These results are presented in figures 25 and 26 for cathodes no. 1 and no. 2, respectively. These data did not correlate as well as those for cathode no. 3. But this is not surprising since cathode geometry is an independent variable that has not been included in equation (15a). Furthermore, these data were not all taken at the low current point when cyclic variations in current existed. The results of figures 25 and 26 demonstrate that these smaller cathodes produced significantly higher ion temperatures than the larger diameter cathodes no. 3. Scatter of the data was such that ion temperature measurements alone could not distinguish between cathodes no. 1 and no. 2. For straight line-fits that intersect the origin in figures 25 and 26, the slope is about 40 percent higher than for cathode no. 3 (fig. 24). But since cathode no. 3 produces more than twice the plasma volume of cathodes no. 1 or 2, its ion heating effectiveness is at least as good as the smaller cathodes.

For helium plasmas, the highest ion temperatures measured were 1725, 1710, and 1350 eV for cathodes no. 1, 2, and 3, respectively. The helium ion temperatures measured in SUMMA (ref. 5) were significantly higher than those reported here for HIP-1. We believe that SUMMA's superior vacuum pumping accounts for the better ion heating.

## Neutron Monitoring Results

When deuterium plasmas were formed, neutrons were produced. Typically the total neutron yield was estimated to be about $10^6$ neutrons per second for cathode voltage and total anode current of 22 kV and 1 A, respectively. The production of neutrons confirms the presence of energetic plasma particles indicated by the Doppler-broadened $H_\alpha$ lines. The functional dependence of neutron count rate was obtained for the following cases: (1) vary G, hold B and V fixed; (2) vary B, hold V and G fixed; (3) vary V, hold B and G fixed; and (4) vary B, hold I and V fixed. Log-log plots of the results of these four cases are shown in figures 27 through 30, respectively. There was no attempt to experimentally determine whether these neutrons came from surface or volume reactions as was done in reference 14. However, the functional dependences presented here provide some insight into the origin of the neutrons.

Volume neutron production rate is proportional to $n_i^2\langle\sigma_{DD}v_i\rangle$, where $\sigma_{DD}$ is the thermonuclear cross section for the $D(d,n)^3He$ reaction and $\langle\sigma_{DD}v_i\rangle$ is the reaction rate averaged over a Maxwellian energy distribution. For the data presented here, the ion temperatures ranged from 100 to 800 eV. At these low temperatures, the reaction rate has a very strong dependence on $T_i$, i.e., $\langle\sigma_{DD}v_i\rangle \propto T_i^9$ (ref. 15). For volume reactions, the neutron count rate therefore has the proportionality

$$N \propto n_i^2\langle\sigma_{DD}v_i\rangle \propto n_i^2 T_i^9 \qquad (16)$$

if changes in plasma volume are ignored. Equation (16) can be used in conjunction with a set of scaling relations to compare the measured neutron count rate with that expected if volume reactions predominated. Since we do not yet have approximate scaling relations for deuterium plasmas, the hydrogen scaling relations (eqs. (12) and (14)) are assumed to apply. Using straight-line fits through the data in figures 27 through 30, simple power-law dependences were obtained. These results are summarized in Table 2 along with the functional relations to be expected if volume neutron reactions predominated. Two out of the four measured results are totally inconsistent with volume reactions. The predicted volume dependences, $N \propto G^{18}$ and $N \propto B^{16}$, are dominated by $T_i^9$. The experimental result $N \propto V^{5.6}$ is interesting because the cross section $\sigma_{DD} \propto \mathcal{E}^{5.5}$ (ref. 16) for particle energy $\mathcal{E}$ in the range of 10 to 20 keV. Ions could acquire energy in this range if they were accelerated to the cathode potential V. The case for I and V constant is of interest because both the measured and predicted N <u>decreased</u> as B increased. Since $T_i$ decreases much slower than $n_i$ increases with increasing B, this result exhibits the strong dependence on $T_i$ that characterizes volume production.

Two out of the four cases studied indicated that volume reactions did not predominate. In the other two cases, the measurements were consistent with the trends predicted for volume reactions. Thus, no conclusion is available from this simplified approach. A more complete experimental program is required to determine the origin of the neutrons. Techniques such as those employed in reference 14, as well as methods to determine the spatial resolution of neutron production should be included.

## CONCLUDING REMARKS

A steady-state hot-ion plasma has been produced and studied in the Lewis HIP-1 facility using water-cooled cathodes. Input power has been at least doubled, and plasma diameter has been increased by a factor of four relative to values with uncooled cathodes.

Independent variables in the experiment were gas flow rate, gas feed location, magnetic field, cathode voltage, electrode geometry, electrode cooling, vacuum pump locations, and vacuum pumping speed. All other plasma parameters were considered as dependent variables, i.e., ion temperature, electron temperature, ion density, neutral gas density, percent dissociation, electric fields, cathode current, anode current, etc. Most of the dependent variables are spatially dependent.

Scaling relations were empirically obtained for ion temperature, electron temperature, relative ion density, and anode current as a function of gas flow rate, magnetic field, and cathode voltage. Typical current versus voltage characteristics were obtained for the discharge. The correlation for ion temperature revealed that ion heating was more effective with two anodes than with one anode. Perhaps the most unexpected result was that ion density scaled inversely with the cube of the cathode voltage. This result was examined from the standpoint of power balance considerations. If charge-exchange power losses are reduced, this adverse effect of cathode voltage on ion density should be mitigated. To reduce the charge-exchange losses, better vacuum pumping may be needed.

Neutron production with deuterium plasmas indicated the presence of energetic particles in the plasma which confirmed the results obtained from the optical monochromator. It was not established whether the neutrons came from the plasma volume or from the surfaces of the electrodes and test section.

# APPENDIX A

## SYMBOLS

| | |
|---|---|
| $A$ | area of wide component of spectral line plot (fig. 9) |
| $B$ | magnetic flux density on the magnetic axis at midplane |
| $\underline{B}$ | magnetic flux density vector |
| $E$ | electric field referred to fixed axes |
| $\underline{E}$ | electric field vector referred to fixed axes |
| $\mathcal{E}$ | ion energy |
| $e$ | absolute value of charge of one electron |
| $G$ | volume rate of flow of gas |
| $I$ | total electric current to both anodes (or to one anode for one anode operation) |
| $k$ | Boltzmann constant |
| $m$ | mass of particle |
| $N$ | neutron count rate |
| $n$ | principal quantum number or neutron |
| $n_e$ | number density of free electrons |
| $n_i$ | number density of $H^+$ ions |
| $n_o$ | number density of $H_2$ neutrals |
| $P$ | input electrical power |
| $p$ | pressure |
| $q$ | power lost by charge-exchange cooling |
| $R$ | reaction rate per unit volume |
| $\underline{r}$ | position vector |
| $T$ | temperature |

| | |
|---|---|
| $V$ | anode-cathode voltage |
| $v$ | velocity |
| $\sigma$ | cross section |
| $\tau$ | characteristic time |

Subscripts:

| | |
|---|---|
| c | charge exchange |
| DD | $D(d, n)^3He$ reaction |
| e | free electron |
| f | fast (or hot or energetic) |
| g | ground state |
| i | ionization or $H^+$ ion |
| o | neutral or $H_2$ |
| p | particle |
| r | ion residence |
| W | energy |
| $\alpha$ | atomic hydrogen Balmer $\alpha$ line |

Special Symbols:

| | |
|---|---|
| $\langle\ \rangle$ | Maxwell-Boltzmann average of included quantity |
| $\overline{\ }$ | line above symbols means radial average across a chord or diameter at the midplane |

# APPENDIX B

## CHARACTERISTIC TIMES

In this Appendix the mean ion residence time and the charge-exchang particle-loss time are defined. Order-of-magnitude estimates are made based on the assumptions: (1) that main volume ionization predominates over ionization at surfaces, in sheaths, and in hollow cathodes; (2) that the main volume of plasma between the two anode rings is approximately homogeneous; and (3) that the neutral background gas is homogeneous and predominantly $H_2$. These times are presented for the same data from which $T_e$ was obtained as given on figures 18 through 21 so that they may be used in conjunction with the discussion of the functional dependences.

Mean ion residence time. - The mean ion residence time $\tau_r$ is the average time that a positive ion remains in the plasma. In this analysis, charge exchange events that do not change the number of positive ions and volume recombination are neglected. The mean ion residence time is the ratio of the total number of positive ions in the plasma to the total rate of production of positive ions, or

$$\tau_r = \frac{\int n_i \, d\underline{r}}{\int R_i \, d\underline{r}} \tag{A1}$$

where $\underline{r}$ is a position vector and $R_i$ is the rate of production of positive ions per unit volume. We assume that equation (A1) can be approximated by

$$\tau_r \approx \frac{\overline{n}_i}{\overline{R}_i} \tag{A2}$$

where $\overline{n}_i$ is the average ion density at the midplane and $\overline{R}_i$ is the average rate of production of positive ions per unit volume at the midplane

$$\overline{R}_i = \overline{n}_o\overline{n}_e\langle\overline{\sigma_{ie}v_e}\rangle + \overline{n}_o\overline{n}_i\langle\overline{\sigma_{ii}v_i}\rangle \tag{A3}$$

where $\sigma_{ii}$ is the cross section for ionization of $H_2$ by protons, $v_i$ is the proton velocity, $\sigma_{ie}$ is the total cross-section for ionization of $H_2$ by electrons, and $v_e$ is the electron velocity. It is reasonable to neglect the concentrations of $H^-$, $H_2^+$, and $H_3^+$ relative to the concentration of $H^+$ (ref. 17), so $\overline{n}_e = \overline{n}_i$. Combining equations (A2) and (A3) give:

$$\tau_r = \frac{1}{\overline{n}_o\left[\langle\overline{\sigma_{ie}v_e}\rangle + \langle\overline{\sigma_{ii}v_i}\rangle\right]} \tag{A4}$$

Values for $\sigma_{ie}$ were obtained from references 18 to 20 and were used to calculate $\langle\sigma_{ie}v_e\rangle$ given in figure 35.

Values for $\sigma_{ii}$ from 2 keV to 140 keV were obtained from references 21 and 22. These were extrapolated from 2 keV down to threshold by means of Massey's expression for the cross section of an inelastic atomic process (ref. 10). The proper value of the threshold is not clear because four or more processes are possible involving the reactions

$$H^+ + H_2 \rightarrow H^+ + H_2^+ + e \tag{VII}$$

$$H^+ + H_2 \rightarrow 2H^+ + H + e \tag{VIII}$$

For reaction (VII) the threshold was calculated from reference 23 to be 23.13 eV laboratory energy. This would also be the threshold of reaction (VIII) if it proceeded by knock-on dissociation or polarization dissociation. However, reaction (VIII) could proceed by electronic excitation to the lowest repulsive state of $H_2^+$. For this case the threshold was estimated from the far turning point of the ground vibrational state of the electronic ground state $H_2$ (ref. 24) and the $H_2^+$ lowest repulsive state potential (ref. 25) and found to be 41.2 eV. For the ion temperatures of this report, values of $\langle \overline{\sigma_{ii} v_i} \rangle$ were found to be insensitive to the choice of threshold and are shown in figure 10. Since $\overline{n}_o$ is a function of G, $\tau_r$ is a function of G, $T_e$, and $T_i$ and is shown in figures 31 to 33. The fractional contribution of $\langle \overline{\sigma_{ii} v_i} \rangle$ to the sum in equation (A4) varied from 0.002 to 0.289 so it cannot be safely neglected.

Charge exchange particle-loss time. - The charge exchange particle-loss time $\tau_{cp}$ is the average time that a positive ion remains in the plasma before undergoing charge exchange. This time is significant because the positive ion is trapped by the magnetic field lines whereas the resulting hot charge-exchange neutral is not trapped and causes serious energy loss from the plasma. The charge-exchange time must be the ratio of the total number of ions in the plasma to the total rate of loss of ions by charge exchange, or

$$\tau_{cp} = \frac{\int n_i \, d\underline{r}}{\int R_{cp} \, d\underline{r}} \tag{A5}$$

where $n_i$ is the number density of ions, and $R_{cp}$ is the charge-exchange rate per unit volume. As before we assume that equation (A5) can be approximated by

$$\tau_{cp} = \frac{\overline{n}_i}{\overline{R}_{cp}} \tag{A6}$$

where the bar indicates a midplane average, and $\overline{R}_{cp}$ is given to a good approximation by

$$\overline{R}_{cp} = \overline{n}_i \overline{n}_o \langle \overline{\sigma_{gc} v_i} \rangle \tag{A7}$$

Substituting equation (A7) into (A6) gives

$$\tau_{cp} = \frac{1}{\overline{n}_o \langle \overline{\sigma_{gc} v_i} \rangle} \tag{A8}$$

Since $\overline{n}_o$ is a function of G, $\tau_{cp}$ is a function of G and $T_i$. Values of $\tau_{cp}$ are shown in figures 31 to 34.

# REFERENCES

1. D. R. Sigman and J. J. Reinmann, "Steady-State Hot-Ion Plasma Produced by Crossed Electric and Magnetic Fields," NASA TM X-2783 (1973).

2. D. R. Sigman, J. J. Reinmann, and M. R. Lauver, " Parametric Study of Ion Heating in a Burnout-Type Device (HIP-1)," NASA TM X-3033 (1974).

3. "Thermonuclear Division Annual Progress Report for Period Ending December 31, 1971," ORNL 4793, Oak Ridge National Lab. (1972), p. 33.

4. A. Hirose, and I. Alexeff, Nuclear Fusion, 12, 315 (1972).

5. J. J. Reinmann, et al., IEEE Trans. Plasma Sci., PS-3, 6 (1975).

6. J. J. Reinmann, et al., "NASA Superconducting Magnetic Mirror Facility," Fifth Symposium on Engineering Problems of Fusion Research (Inst. Electronics and Electrical Engrs. New York, 1974), p. 587.

7. J. J. Reinmann, et al., Bull. Amer. Phys. Soc., 19, 874 (1974), Abstract 2D16.

8. The water-cooled cathode was suggested, designed, and fabricated by R. J. Tashjian at NASA Lewis Research Center.

9. R. W. Patch, D. E. Voss, and J. J. Reinmann, "Ion and Electron Temperatures in the SUMMA Mirror Device by Emission Spectroscopy," presented at Sixteenth Annual Meeting of the Plasma Physics, (Alberquerque, New Mexico, Oct. 28-31, 1974).

10. W. R. Hess, Phys. Ltrs., 41A, 66 (1972).

11. W, H. Cramer, J. Chem. Phys., 35, 836 (1961).

12. S. K. Allison, Rev. Mod. Phys., 30, 1137 (1958).

13. R. V. Neidigh, Oak Ridge National Lab., personal communication.

14. I. Alexeff, W. D. Jones, and R. V. Neidigh, Phys. Rev. Ltrs., 18, 1109 (1966).

15. B. N. Kozlov, Soviet J. Atomic Energy, 12, 247 (1962).

16. S. Glasstone and R. N. Loveberg, "Controlled Thermonuclear Reactions" (D. Van Nostrand Co., Inc., Princeton, N.J., 1960), p. 17.

17. R. Krawec, "Steady-State Composition of a Low-Density Nonequilibrium Hydrogen Plasma," NASA TN D-3457 (1966).

18. D. Rapp and P. Englander-Golden, J. Chem. Phys., 43, 1464 (1965)

19. J. T. Tate and P. T. Smith, Phys. Rev., 39, 270 (1932).

20. B. L. Schram, et al., Physica, 31, 94 (1965).

21. F. J. de Heer, J. Schutten, and H. Moustafa, Physica, 32, 1766 (1966).

22. O. Hollricher, Z. fur Physik, 187, 41 (1965).

23. R. W. Patch, J. Quant. Spectrosc. Radiat. Transfer, 9, 63 (1969).

24. R. J. Spindler, Jr., J. Quant. Spectrosc. Radiat. Transfer, 9, 597 (1969).

25. D. R. Bates, K. Ledsham, and A. L. Stewart, Phil. Trans. Roy. Soc. Lond., A246, 215.(1954).

## TABLE I. - CATHODE AND ANODE DIMENSIONS (IN CENTIMETERS)

| Cathode | | | Anode | | Annular gap |
|---|---|---|---|---|---|
| | i. d. | o. d. | Helix i. d. | Tube diameter | |
| No. 1 | 1.35 | 2.86 | 4.30 | 0.64 | 0.87 |
| No. 2 | 1.90 | 2.86 | 4.60 | .64 | .87 |
| No. 3 | 2.54 | 4.45 | 6.35 | .95 | .95 |
| Tungsten | .95 | 1.27 | 2.86 | .64 | .80 |

# TABLE II. - FUNCTIONAL DEPENDENCE OF NEUTRON COUNT RATE

| Experimental result | Predicted dependence using H scaling $N \propto n_i^2 \langle \sigma_{DD} v_i \rangle \propto n_i^2 T_i^9$ | Independent variables held constant |
|---|---|---|
| $N \propto G^{3.7}$ | $N \propto G^{18}$ | B, V |
| $N \propto B$ | $N \propto B^{16}$ | V, G |
| $N \propto V^{5.6}$ | $N \propto V^{6.4}$ | B, G |
| $N \propto B^{-0.5}$ | $N \propto B^{-0.2}$ | I, V |

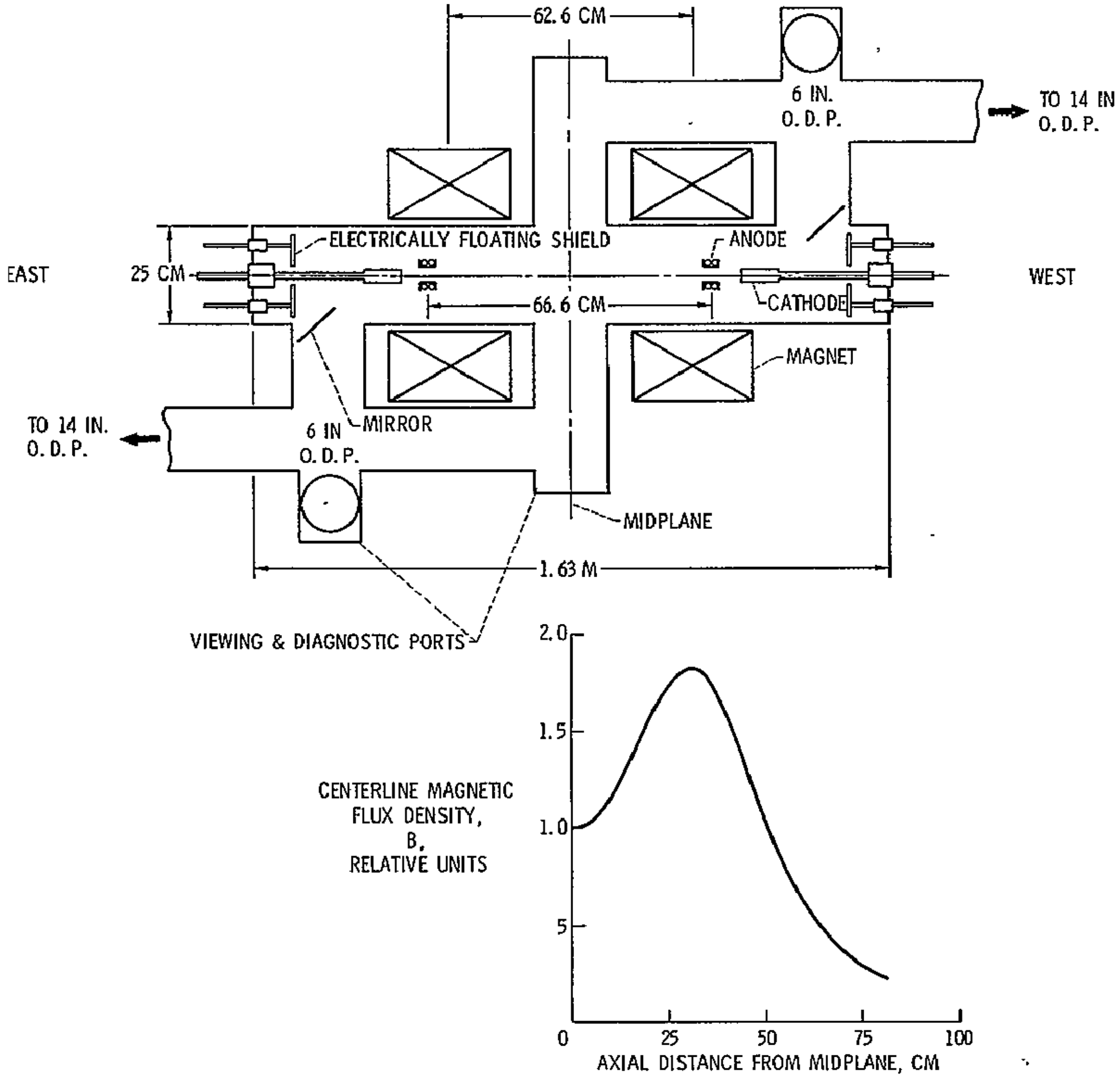

Figure 1. - Test section and magnetic field configuration.

E-8588

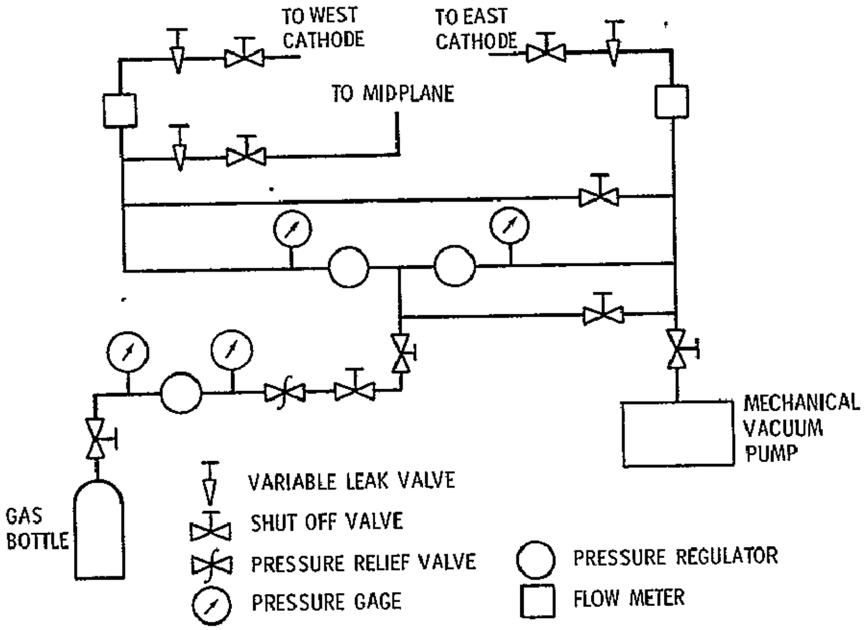

Figure 2. - HIP-1 gas fuel system.

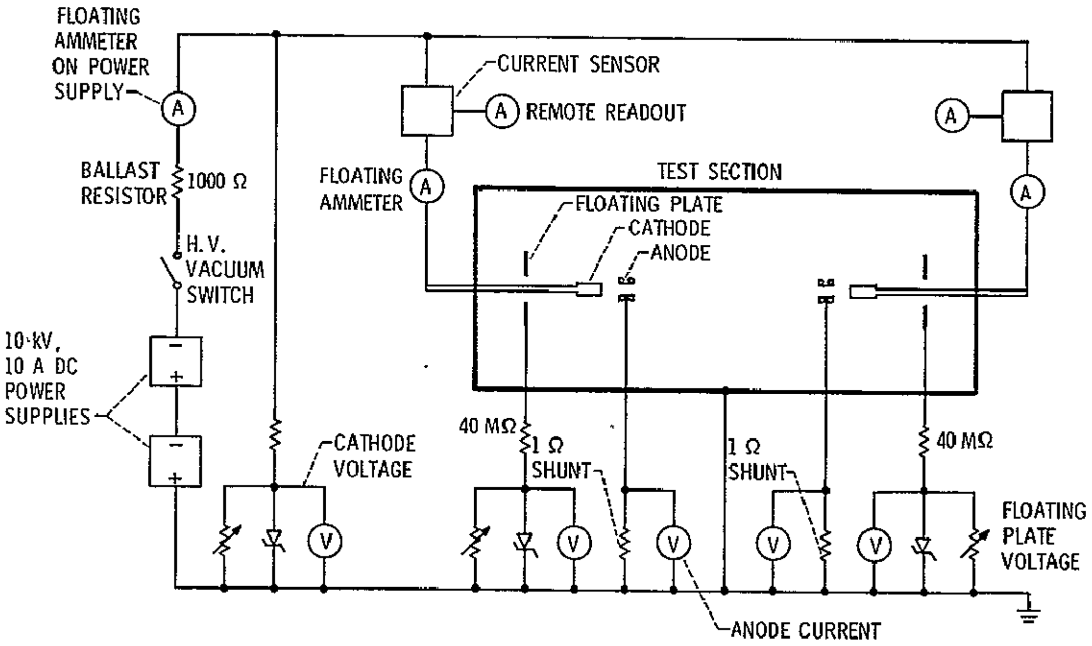

Figure 3. - HIP-1 high voltage schematic.

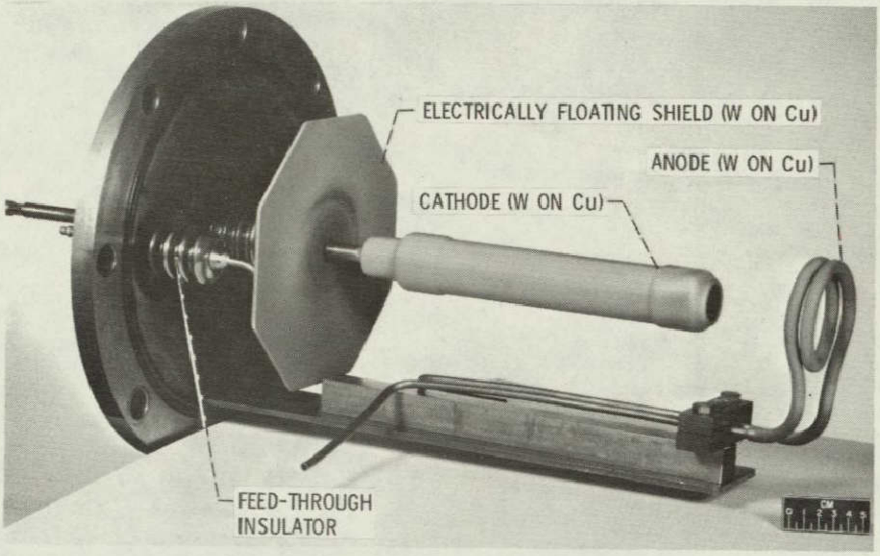

Figure 4. - HIP-1 electrode assembly.

E-8588

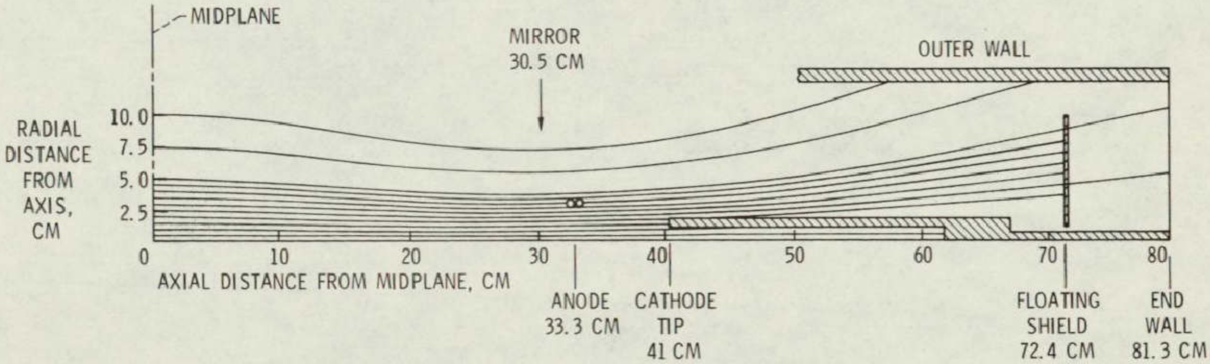

(CATHODE NO. 3 WATER COOLED)

Figure 5. - Magnetic field-line plot showing location of electrodes.

Figure 6. - HIP-1 cathodes.

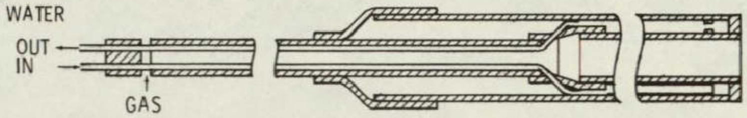

WATER COOLED NO. 1, 1.3 CM I.D., 2.9 CM O.D.

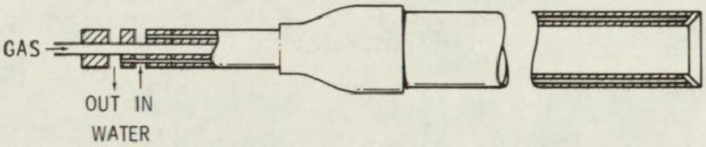

WATER COOLED NO. 2, 1.9 CM I.D., 2.9 CM O.D.

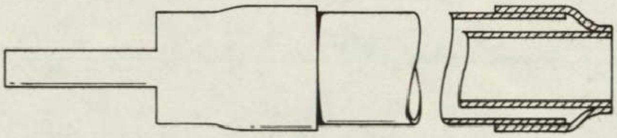

WATER COOLED NO. 3, 2.5 CM I.D., 4.4 CM O.D.

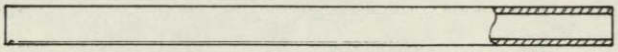

UNCOOLED TUNGSTEN, 1.0 CM I.D., 1.3 CM O.D.

Figure 7. - Cut-away views of HIP-1 cathodes.

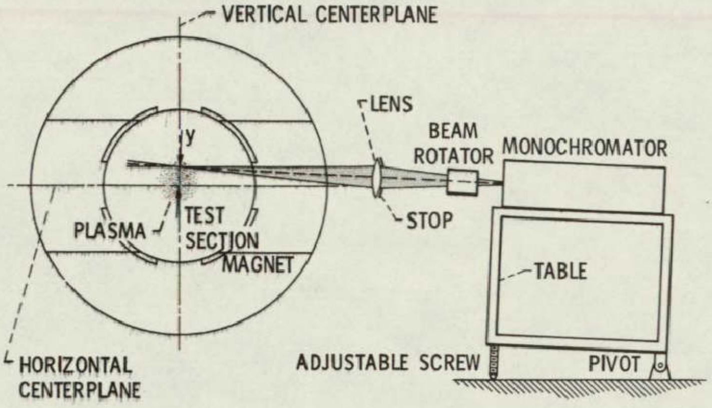

CS-69934

Figure 8. - Apparatus for optical spectroscopic diagnostics. Not to scale.

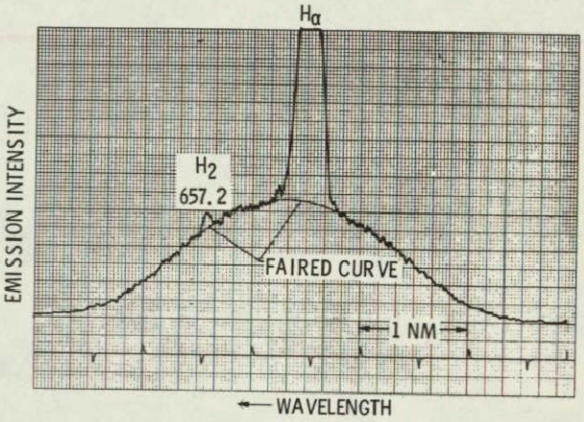

Figure 9. - Typical $H_\alpha$ line exhibiting wide and narrow components.

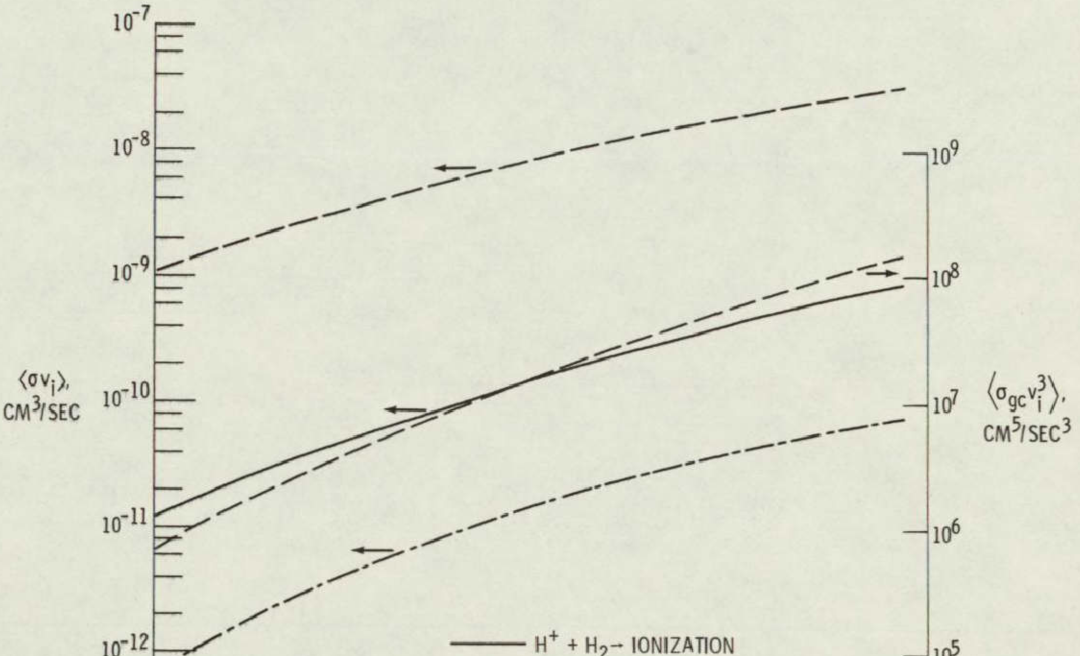

Figure 10. - Maxwell averages for reaction rates, $\langle \sigma v \rangle$, for three processes and $\langle \sigma v^3 \rangle$ for one process.

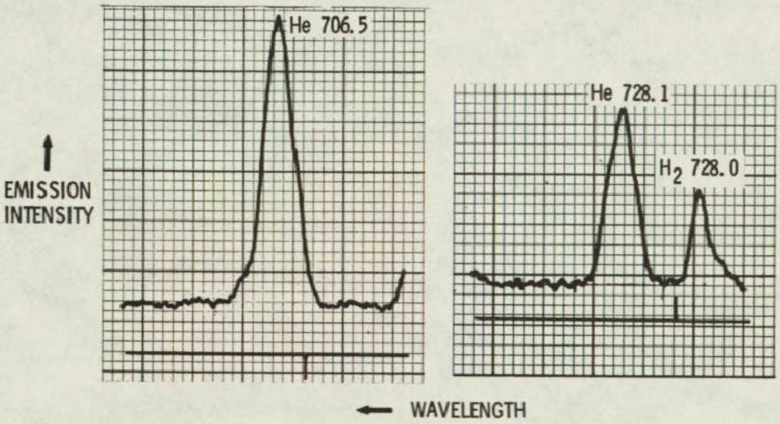

Figure 11. - Typical He 706.5 and 728.1 nm line emission from a $H_2$-He mixture used to obtain average electron temperature.

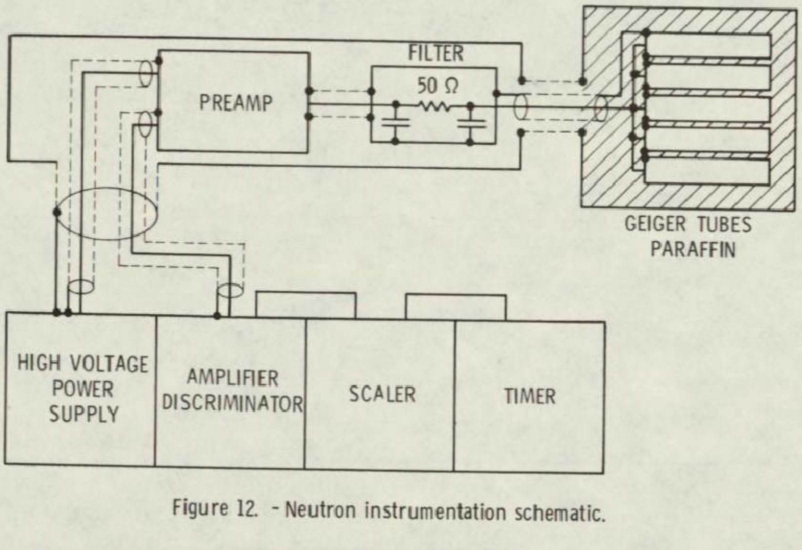

Figure 12. - Neutron instrumentation schematic.

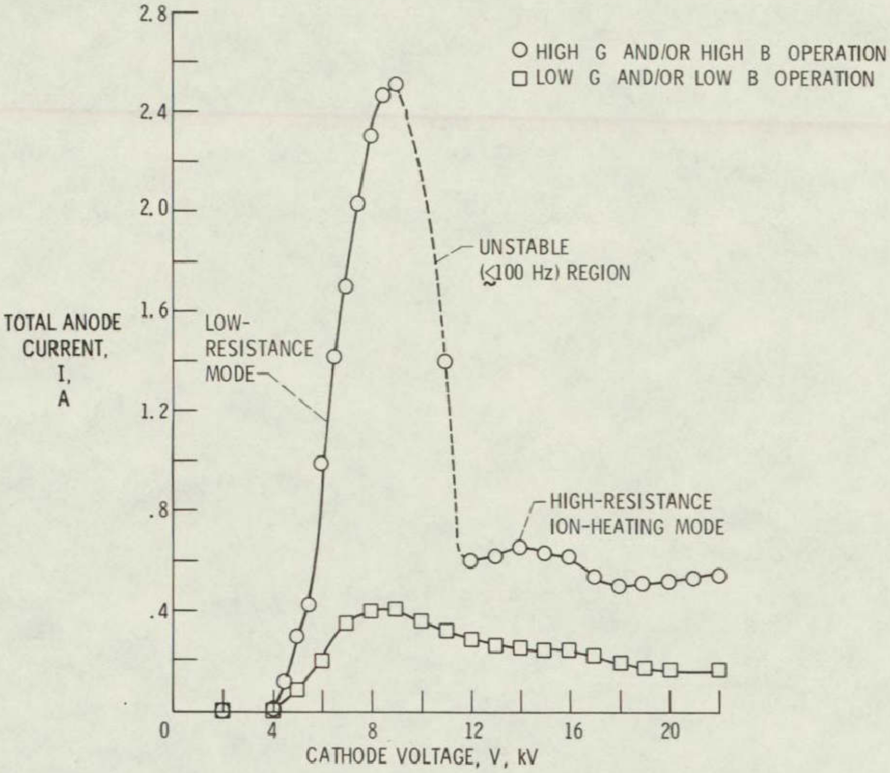

Figure 13. - Typical current versus voltage curves.

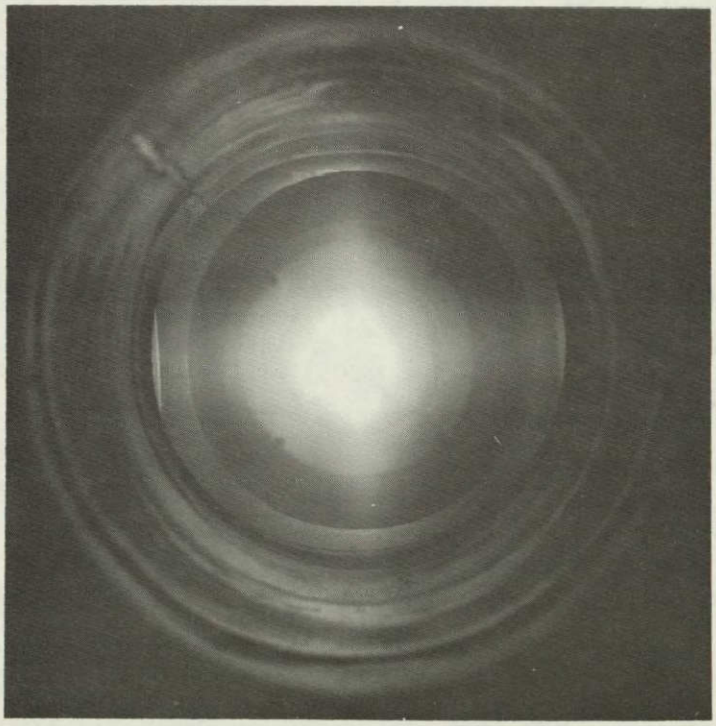

Figure 14. - HIP-1 hydrogen plasma as seen from mid-plane viewing port.

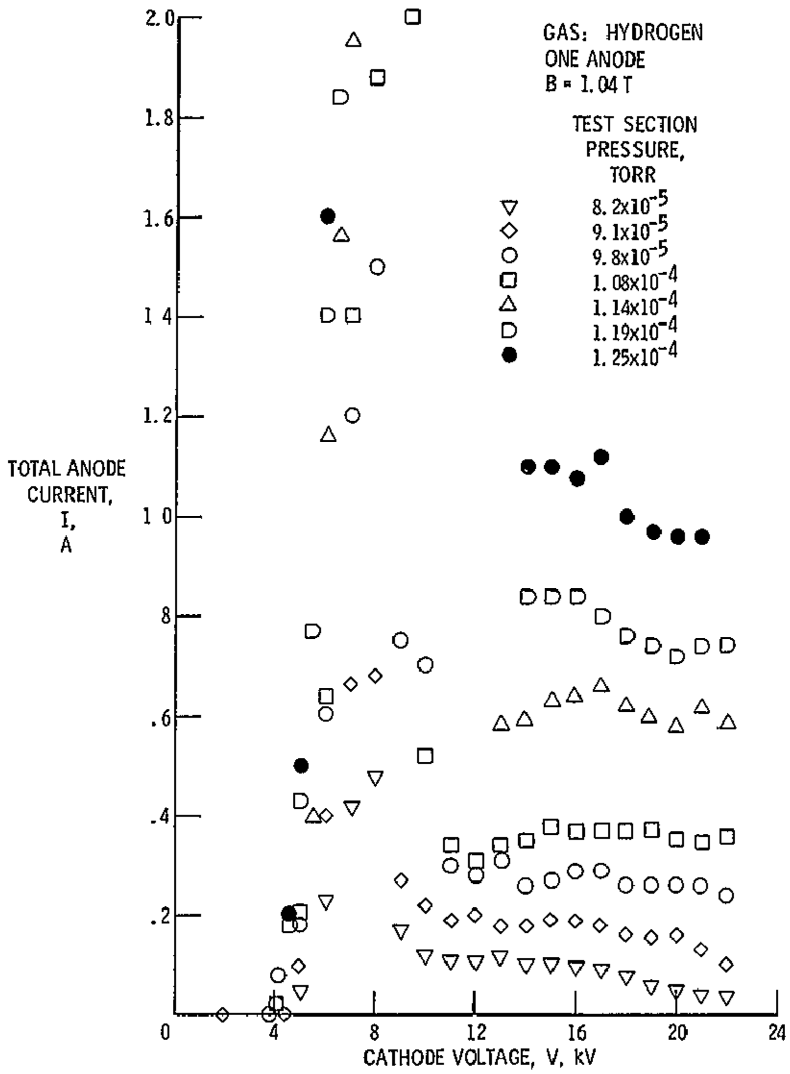

Figure 15. - Effect of gas flow rate on the current versus voltage curves.

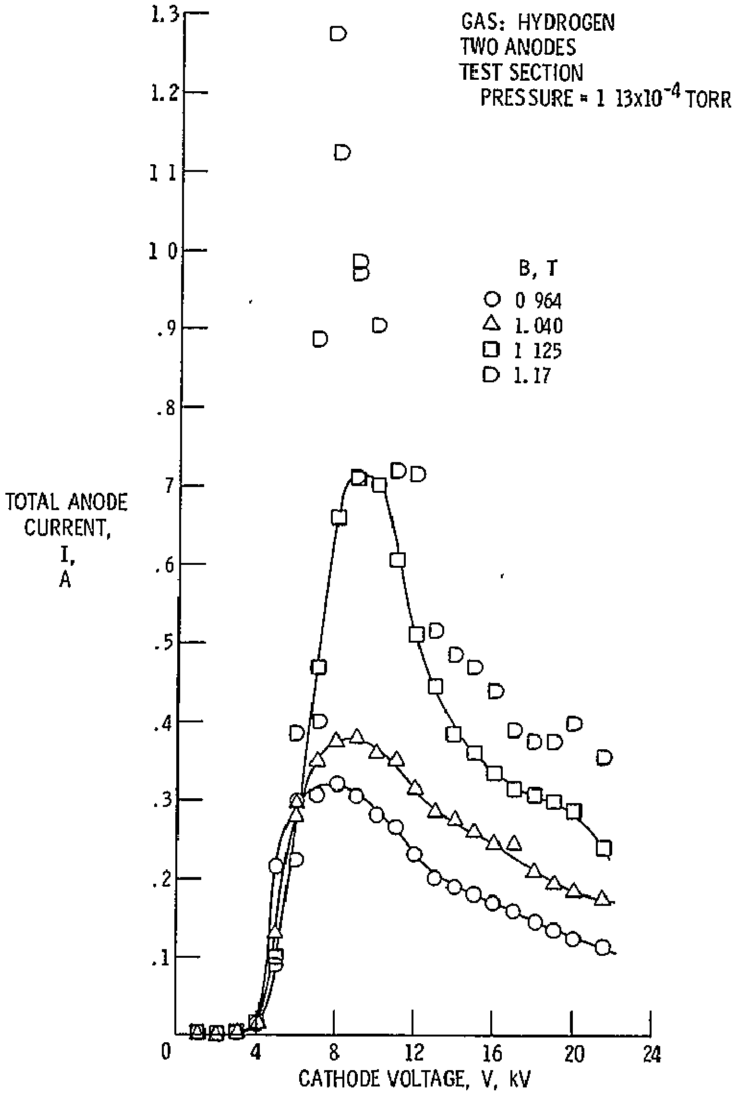

Figure 16. - Effect of magnetic flux density on current versus voltage curves.

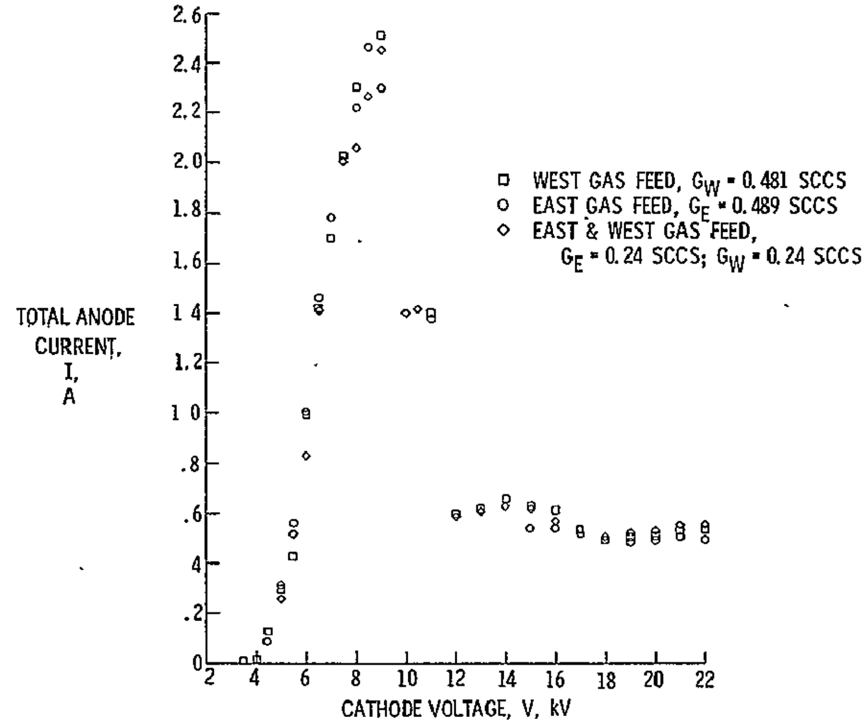

Figure 17. - Effect of gas feed location on current versus voltage curves.

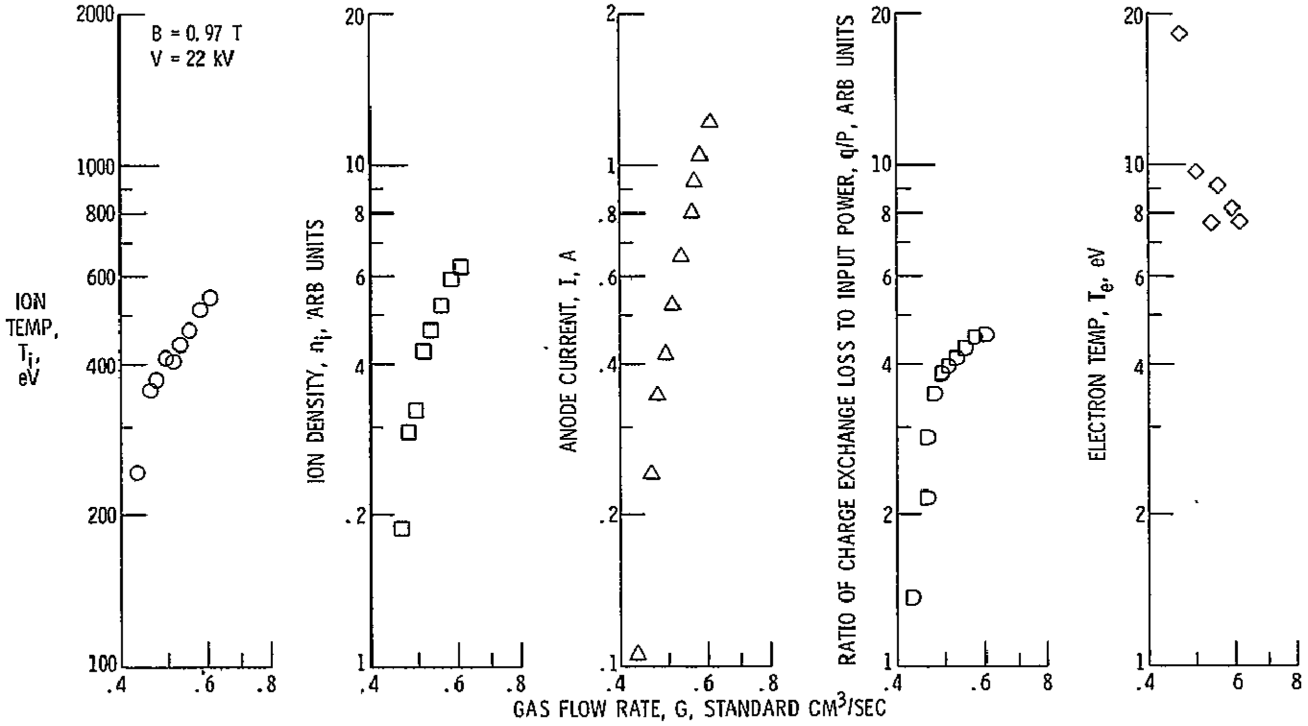

Figure 18. - Effect of gas flow rate on key variables with B and V held constant.

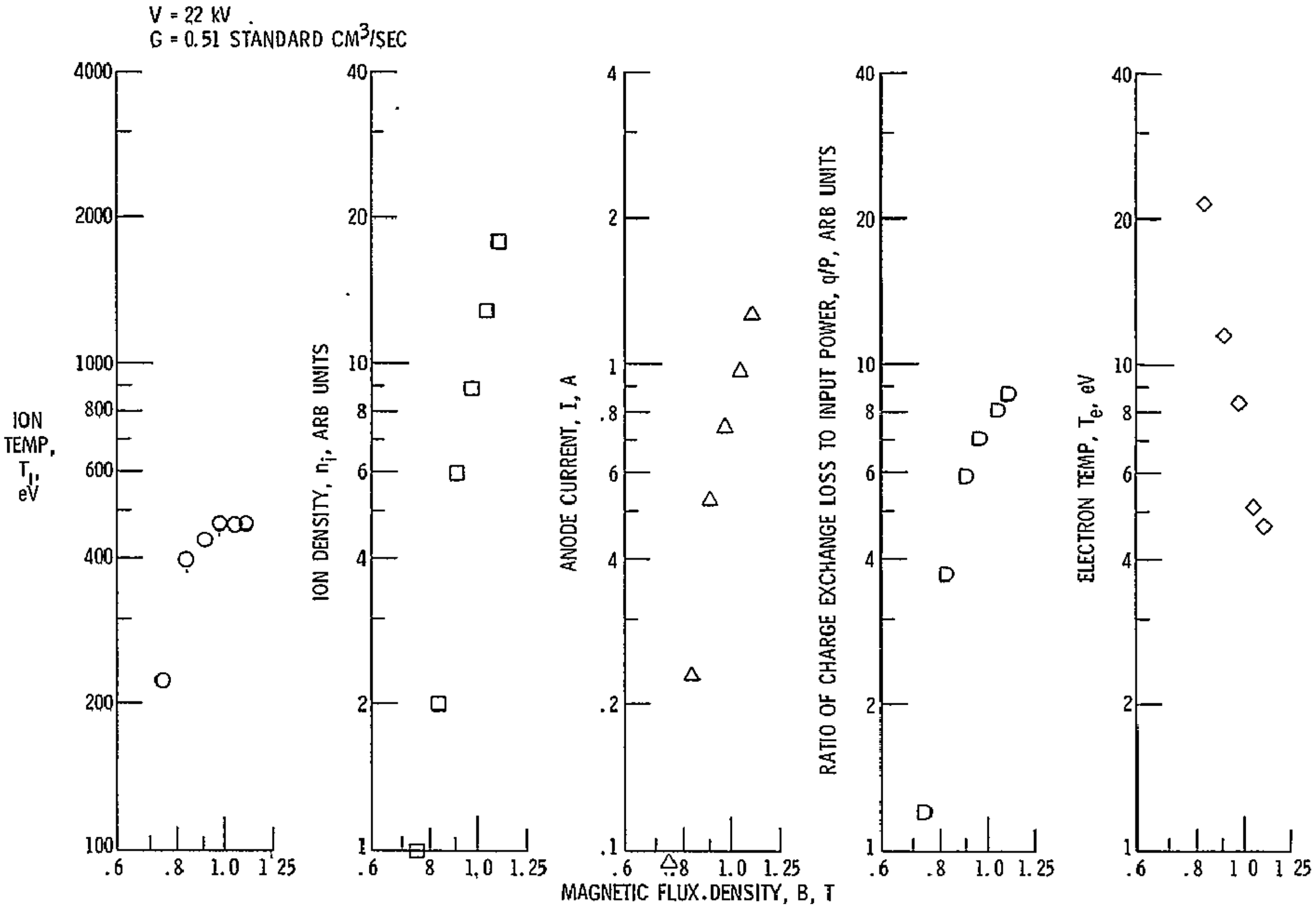

Figure 19. - Effect of magnetic flux density on key variables with V and G held constant.

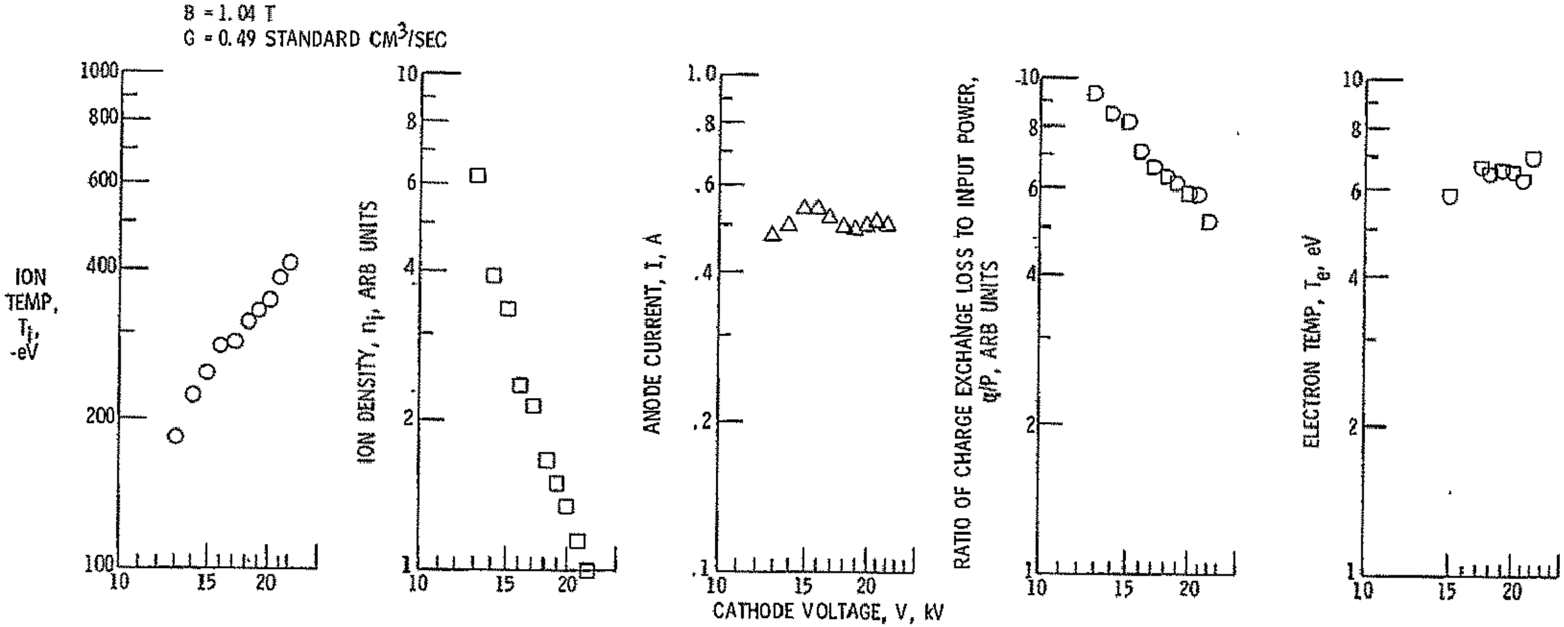

Figure 20(a). - Effect of cathode voltage on key variables with G and B held constant

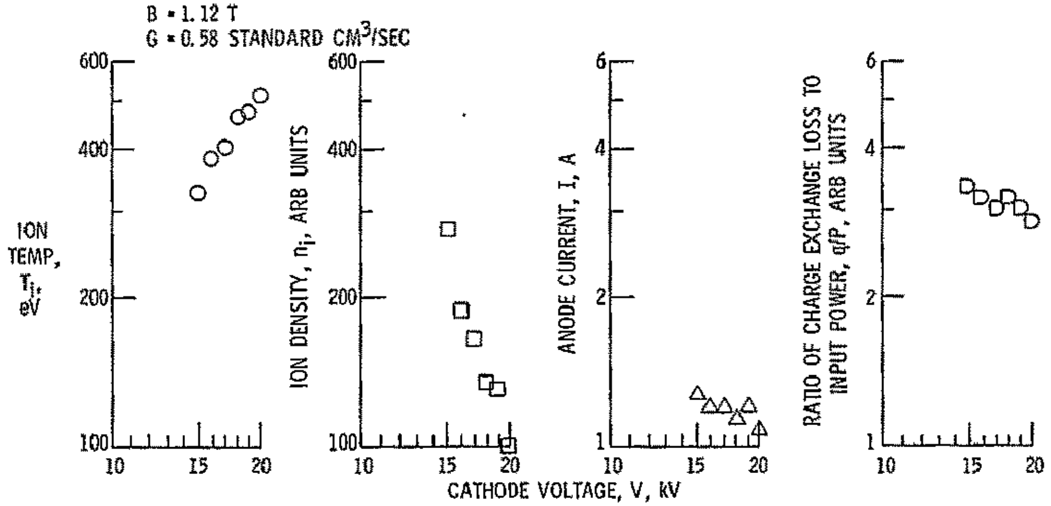

Figure 20(b). - Effect of cathode voltage on key variables with G and B held constant.

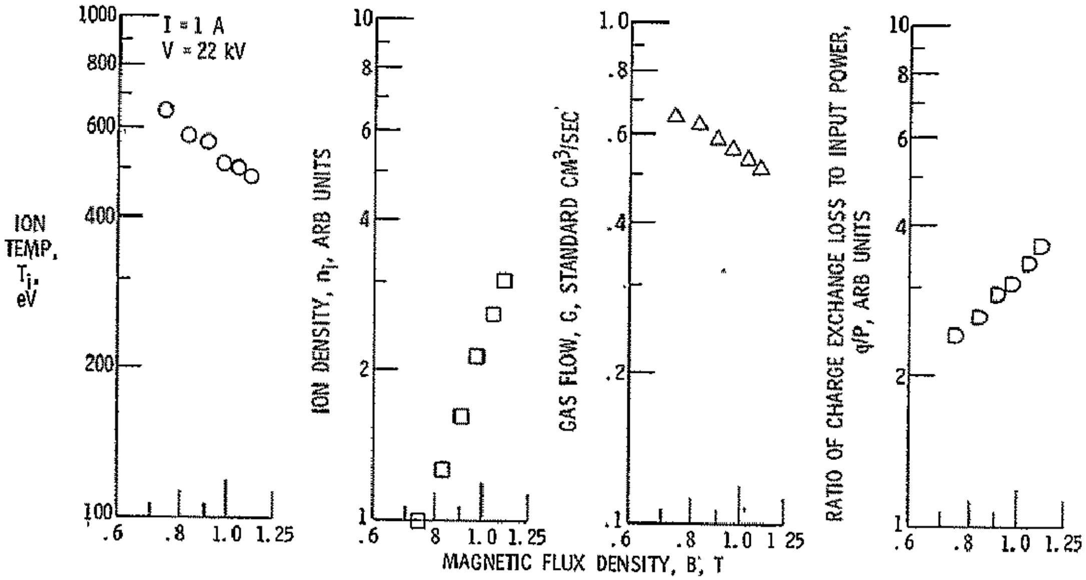

Figure 21. - Effect of magnetic flux density on key variables with I and V held constant.

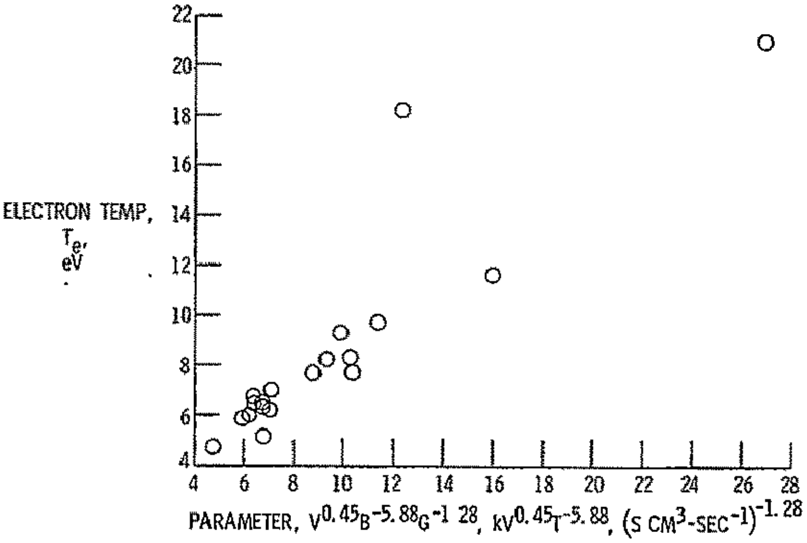

Figure 22. - Correlation of average electron temperature for water-cooled cathodes no. 3 with one anode.

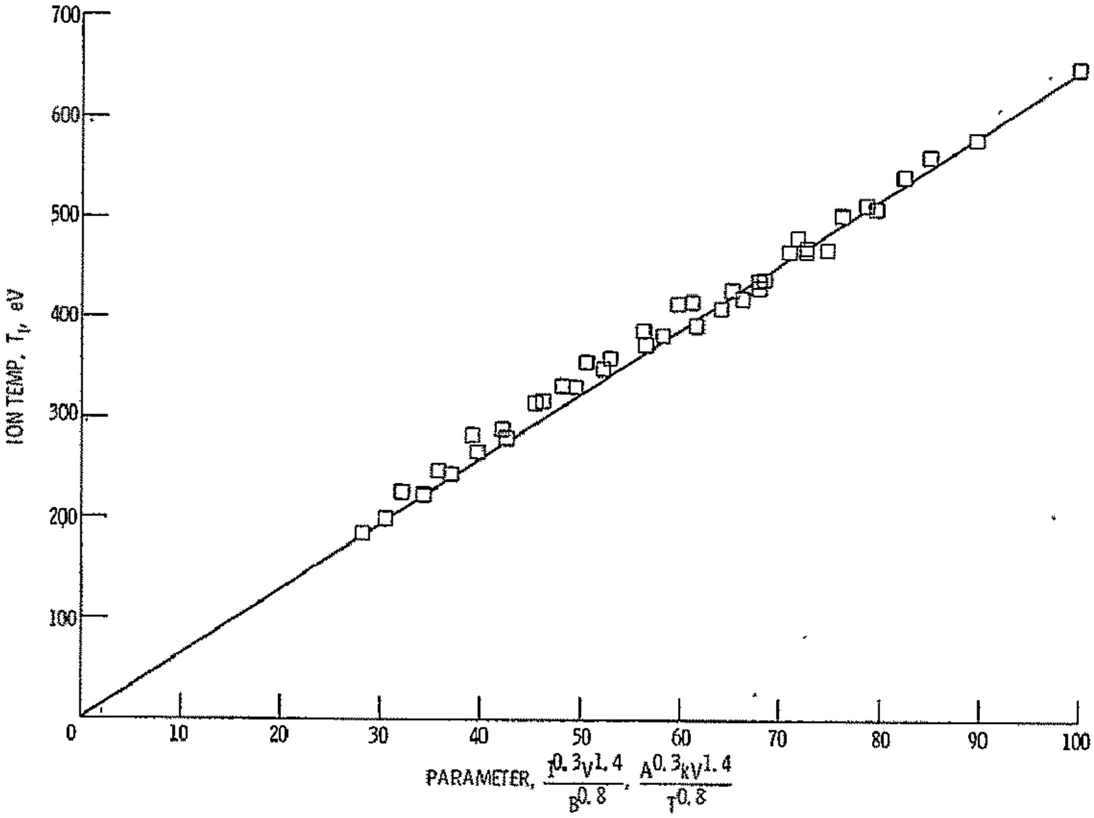

Figure 23. - Correlation of average $H^+$ ion temperature for water-cooled cathodes no. 3 with one anode and gas feed into west cathode only.

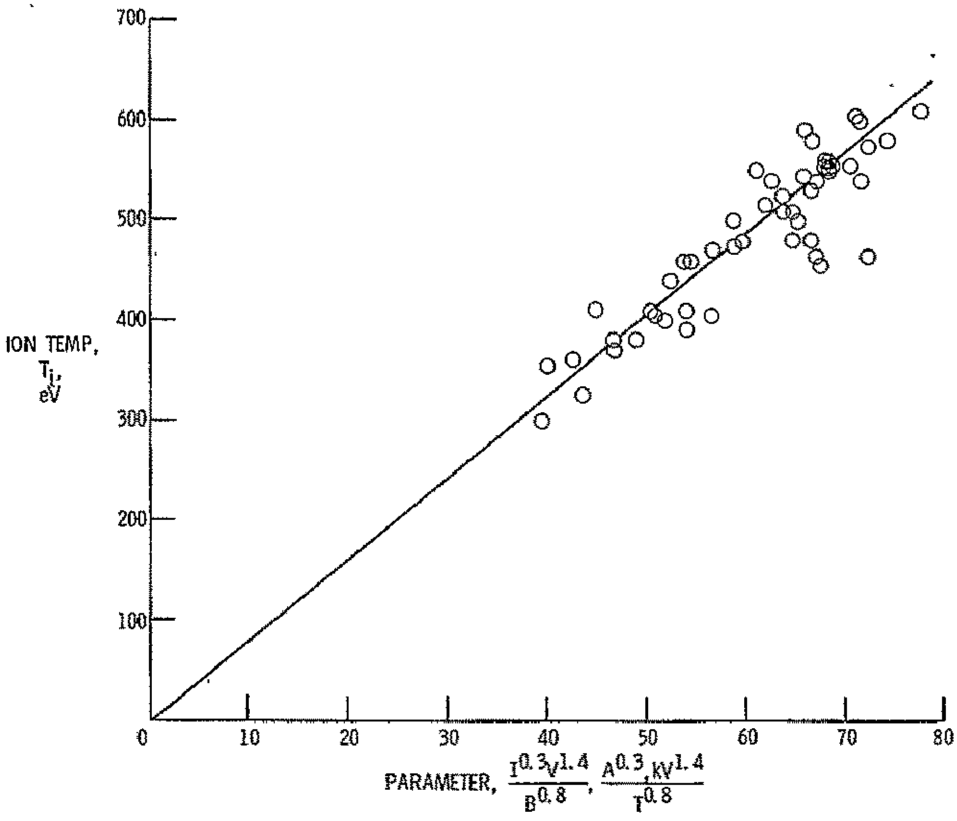

Figure 24. - Correlation of average $H^+$ ion temperature for water-cooled cathodes no. 3 with two anodes.

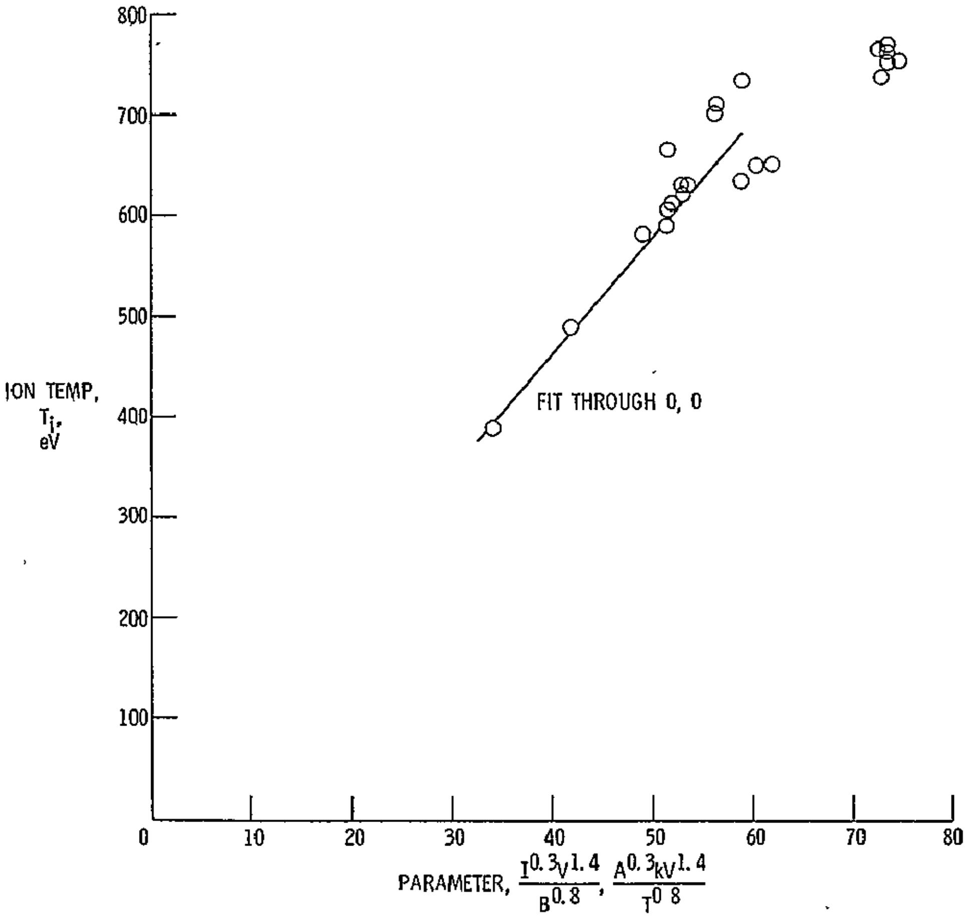

Figure 25. - Correlation of average $H^+$ ion temperature for water-cooled cathodes no. 1 with two modes.

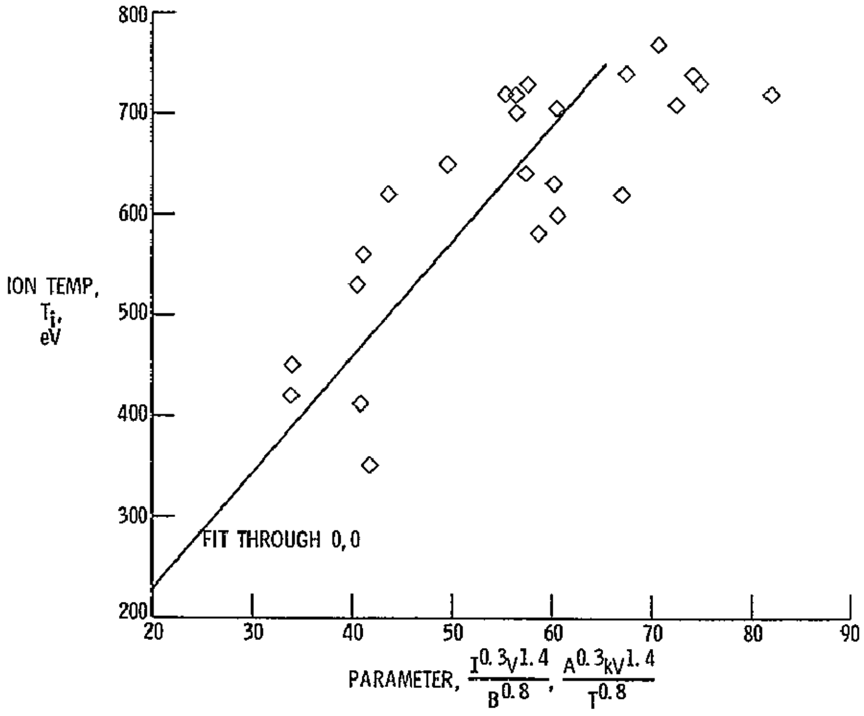

Figure 26. - Correlation of average $H^+$ ion temperature for water-cooled cathodes no. 2 with two anodes.

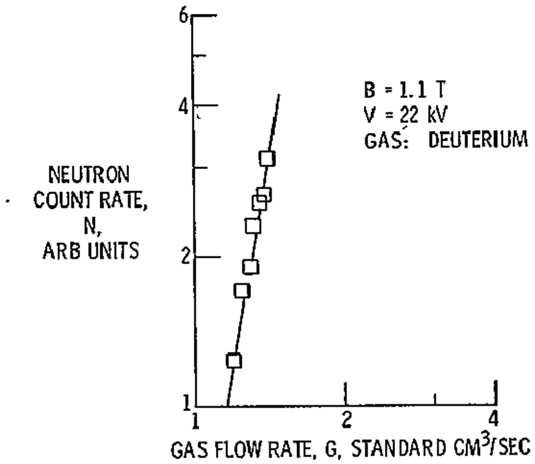

Figure 27. - Neutron count rate as function of gas flow rate with B and V held constant.

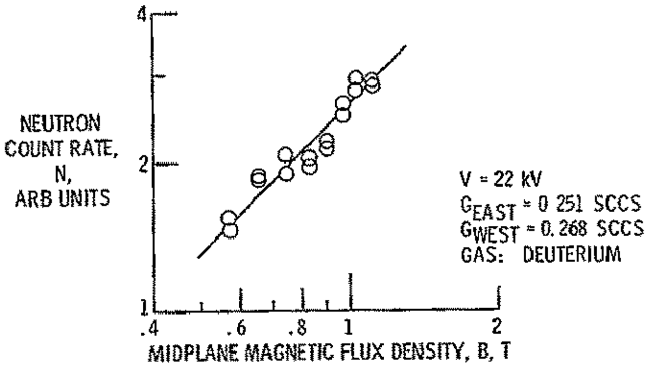

Figure 28. - Neutron count rate as function of midplane magnetic flux density with V and G held constant.

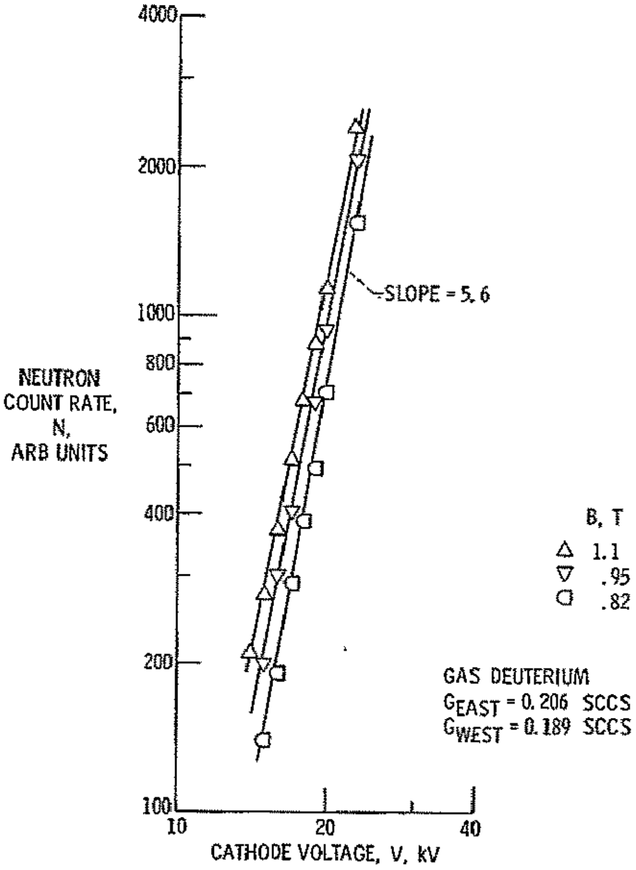

Figure 29. - Neutron count rate as function of cathode voltage with B as parameter and G held constant.

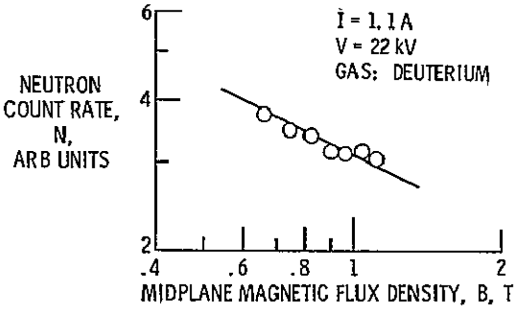

Figure 30. - Neutron count rate as function of midplane magnetic flux density with I and V held constant.

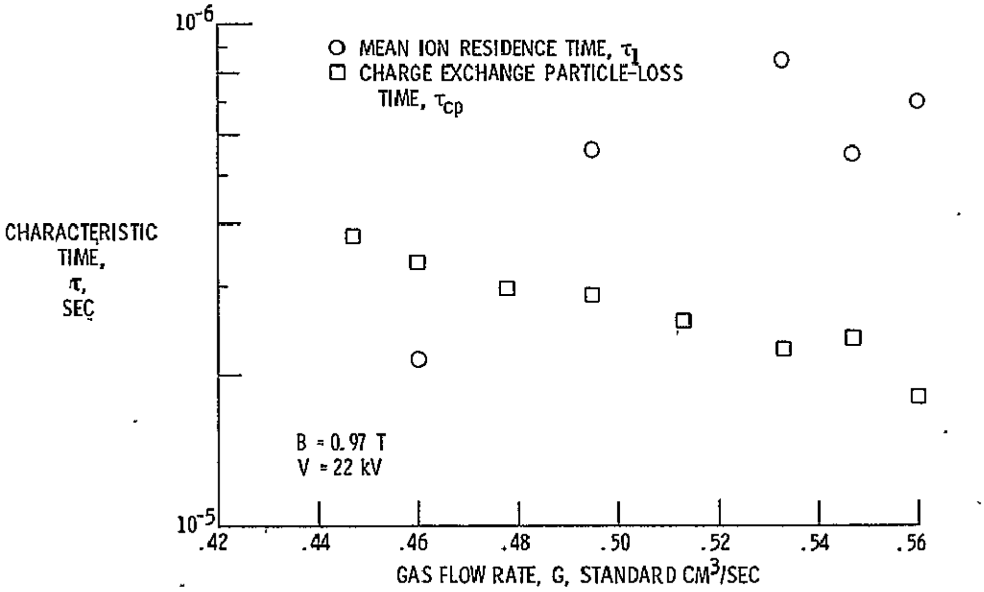

Figure 31. - Effect of gas flow rate on characteristic times with B and V held constant.

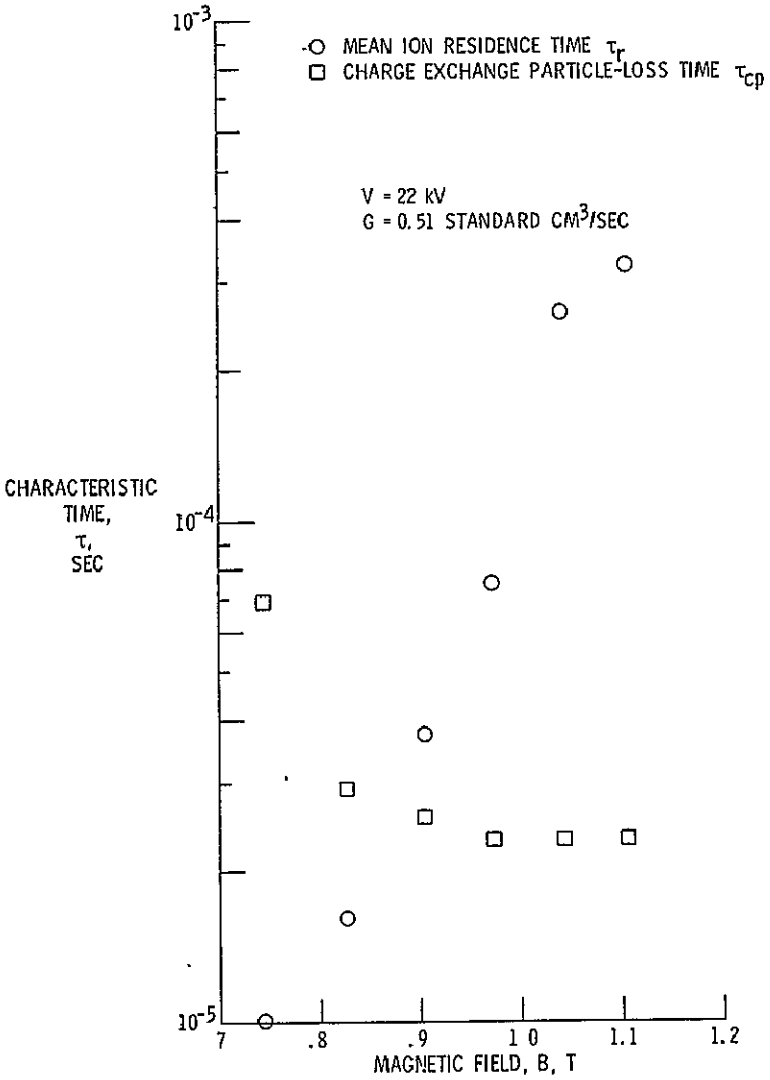

Figure 32. - Effect of magnetic field on characteristic times with V and G held constant.

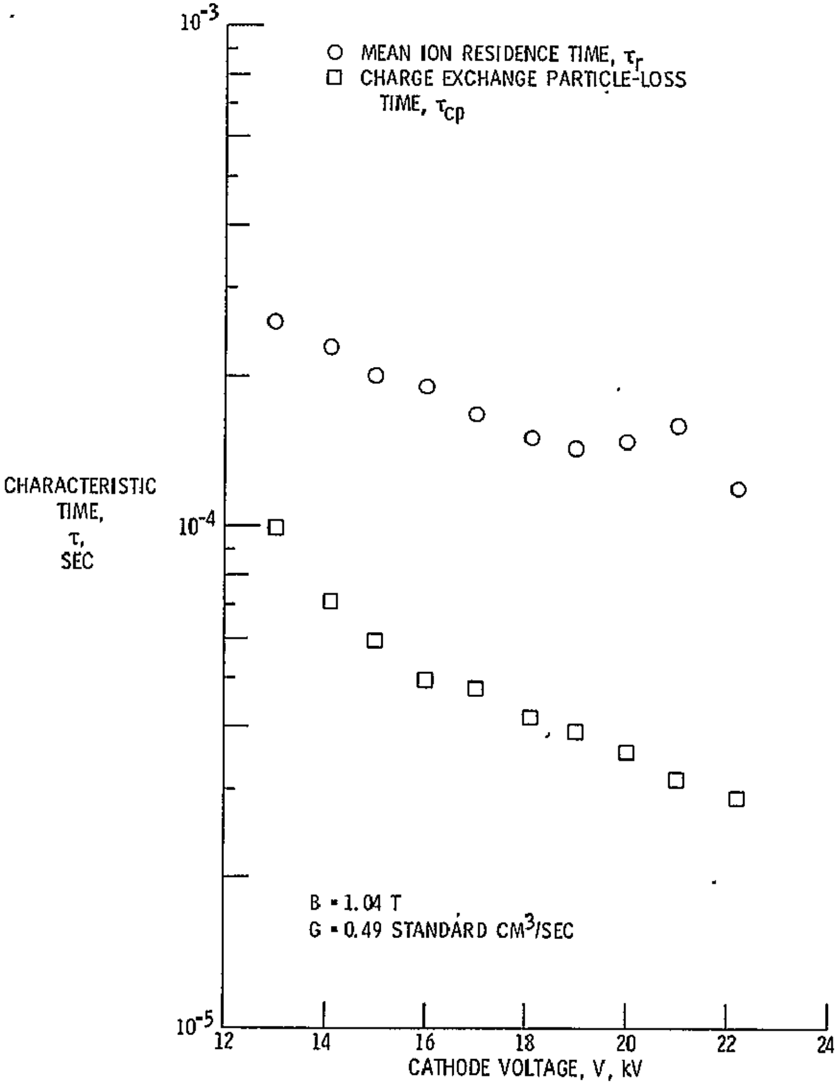

Figure 33. - Effect of cathode voltage on characteristic times with G and B held constant.

E-8588

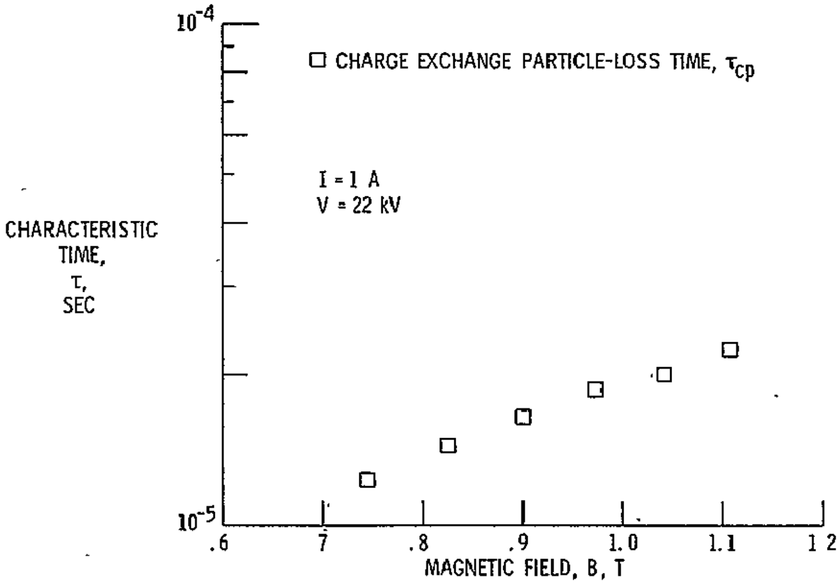

Figure 34. - Effect of magnetic field on characteristic times with I and V held constant.

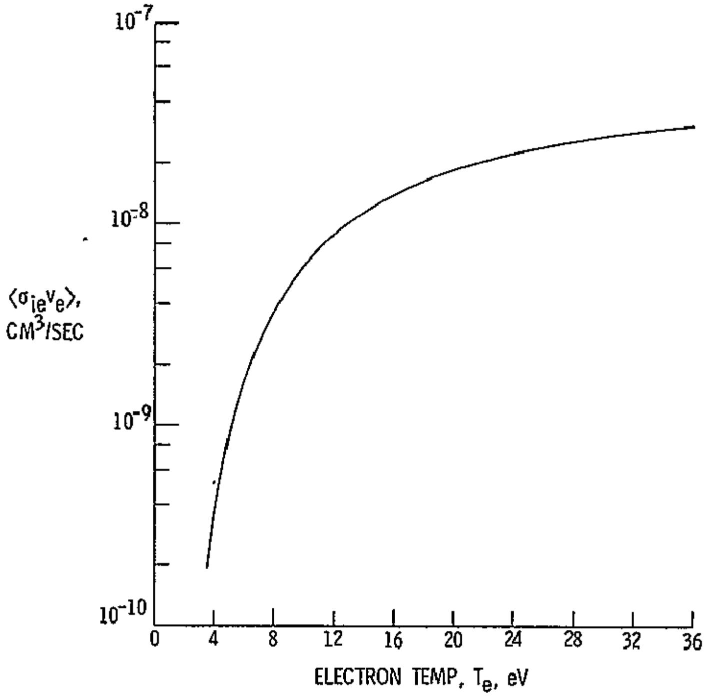

Figure 35. - Maxwell averages for reaction rate, $\langle\sigma_{ie}v_e\rangle$, for electrons colliding with $H_2$ and producing ionization.